

The pseudogap phase in high-temperature superconductors

An angle resolved photo emission spectroscopy study

Masterthesis

Christian Matt

Department of Physics, ETH Zürich in collaboration with PSI, Villigen

cmatt@student.ethz.ch

Supervisor: Dr. Johan Chang & Prof. Dr. J. Mesot

July 25, 2012

Abstract

High-resolution angle-resolved photoemission spectroscopy (HR-ARPES) was performed on $\text{La}_{1.6-x}\text{Sr}_x\text{Nd}_{0.4}\text{CuO}_4$ (Nd-LSCO) single crystals to study low energy excitations in the pseudogap phase. The study of the Fermi surface (FS) revealed a change of its character from hole-like to electron like at $x \approx 0.20$. The FS area was found to fulfill expectations of Luttinger's theorem. The temperature dependence of Δ^* was measured in the antinodal (1,0) region. The momentum dependent study of the pseudogap, Δ^* , revealed a striking difference from $d_{x^2-y^2}$ - wave symmetry which was found to apply for the superconducting gap. A locus of gapless quasiparticles known as the Fermi arc with doping dependent length was observed. A doping dependent investigation of Δ^* revealed the closing of the pseudogap within the superconducting dome. The results of the momentum and k -dependence were interpreted within the scenario where the pseudogap is competing with superconductivity.

Contents

1	Introduction	3
1.1	Principles of Angular Resolved Photoemission Spectroscopy	4
1.2	Scattering theory	6
2	Experimental Methods: Measurement setup - sample preparation	10
2.1	Experimental setup - ARPES applied	10
2.2	Cuprate Compounds	11
2.2.1	Crystal structure	11
2.2.2	Sample preparation	12
2.3	Calibration and Normalization of ARPES spectra	13
2.4	Analyzing ARPES data	15
2.4.1	MDC and EDC method	15
2.4.2	Conversion from detector angles into k -space	18
3	The Fermi surface of Nd-LSCO	20
3.1	Evolution of the Fermi surface - Introduction	20
3.2	The FS of Nd-LSCO	21
3.2.1	Results	21
3.2.2	Analysis of the FS	22
4	The gap in the normal state	25
4.1	Introduction	25
4.2	Lineshape of the the EDC in antinodal region	26
4.2.1	Antinodal ARPES spectra	26
4.2.2	Raw energy distribution curves	27
4.2.3	Symmetrized EDC - Analysis	28
4.3	Momentum dependence of the pseudogap	29
4.4	Temperature dependence of the pseudogap	31
4.4.1	Introduction	31
4.4.2	Result: Δ^* in Nd-LSCO, $x = 0.20$	32
4.4.3	Analysis	32
4.4.4	Vacuum issues and self surface doping	32

4.4.5 Outlook	33
5 Conclusion	34

Chapter 1

Introduction

In modern condensed matter physics, strongly correlated electron systems are of great interest and intense research is done in this direction. Strong efforts were especially done in investigations on high-temperature superconductors (HTSC), first discovered in 1986 by Bednorz and Müller [1]. These systems, which are found to emerge out of a strongly correlated metallic phase are still poorly understood and the mechanism of HTSC has eluded research for nearly 3 decades. Also, the pseudogap phase in underdoped cuprates is a problem that had defied a solution and had lead to big controversy. Especially its connection to superconductivity, whether its a pre-superconducting phase or a competing phase is heavily debated. A lot of experimental techniques like resistivity, Nernst effect, Andreev reflection and spectroscopy have been applied to tackle this question - so far without resounding success. Here we attack the problem with employing angle resolved photoemission spectroscopy (ARPES).

To have access to the pseudogap phase in a wide doping and temperature region we were searching for a material with a strongly suppressed superconducting dome. This allows us to investigate the pseudogap phase at very low temperatures which leads to enhanced energy resolution due to lower thermal broadening effects.

The material which we propose is $\text{La}_{1.6-x}\text{Sr}_x\text{Nd}_{0.4}\text{CuO}_4$ (Nd-LSCO), a hole doped cuprate superconductor with two dimensional layered structure. The ARPES technique has special strength in two dimensional structures. The weakly coupled layers allow to cleave the sample inside the ultra high vacuum (UHV) of the ARPES chamber. Providing a nice and clean surface is essential for successful ARPES experiment being a very surface sensitive technique. Vice versa, the ARPES experiment at a 3rd generation synchrotron provides high photon flux, variable polarizations and a wide energy range of the photon beam for significant measurements on this complex material.

This Thesis is organized as follows: Following, an introduction into the principles of photoemission theory and scattering theory will give more insights into this technique and its application. In the second chapter, a description of the compound and the whole procedure of

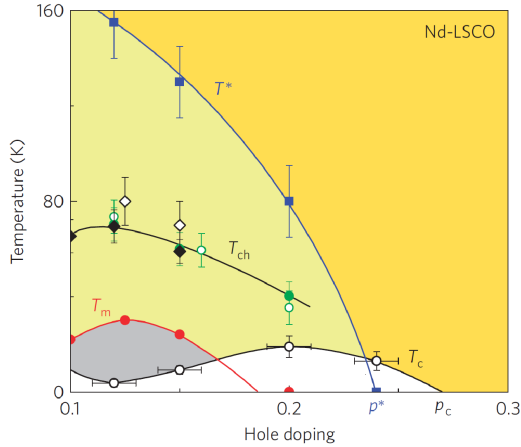


Figure 1.1: Temperature-doping phase diagram of Nd-LSCO. The pseudogap respectively superconducting phase is located below T_c respectively T^* . T_c and T^* were determined by resistivity measurements by Daou *et al.*. T_m and T_{ch} denote the onset temperatures for static magnetism and charge ordering measured by zero-field μ SR respectively X-ray diffraction. Adapted from Daou *et al.* [4].

sample preparation and ARPES measurement including some analyzing techniques specifies the requirements of this experiment. The results will be presented in chapter 3 by the measurement and discussion of the Fermi surface and in chapter 4 by the gap measured for temperatures above T_c (normal state). The conclusion in chapter 5 will summarize the results of this work and give an outlook for possible following experiments.

1.1 Principles of Angular Resolved Photoemission Spectroscopy

The photoelectric effect is known and has been used in experimental physics for far over a century and lead to great achievements, especially in the wide field of condensed matter physics. For the first time observed by H. Hertz in 1887, this effect could be explained by A. Einstein in 1905 by the quantization of light into individual particles which are nowadays known as photons. Einstein found that each of these photons is carrying the energy $h\nu$ with ν being the photon frequency and h Planck's constant. When a metal is illuminated by light of a certain (high enough) frequency ν , electrons will be ejected with a well defined kinetic energy. Using the energy conservation law, the kinetic energy of non-interacting electrons is defined as:

$$E_{\text{kin}} = h\nu - \phi - |E_B| \quad (1.1)$$

The variable ϕ is the minimum energy of the electron required to escape the sample, *i.e.* the work-function of the sample and E_B denotes the binding energy inside the crystal. A

schematic of the energetics of a direct transition in an ARPES experiment is presented in fig. 1.2. Directly connected to the kinetic energy of the electron is the absolute value of its momentum $p = \sqrt{2mE_{\text{kin}}}$; where m is the electron mass. Under the reasonable assumption of a semiinfinite crystal with translational symmetry parallel to the crystal-surface, the momentum parallel to the surface, \mathbf{p}_{\parallel} , is conserved. It is determined by the help of the photoemission geometry which is sketched in fig. 1.3:

$$\mathbf{p}_{\parallel} = \hbar\mathbf{k}_{\parallel} = \sqrt{2mE_{\text{kin}}} \sin \vartheta \begin{pmatrix} \cos \phi \\ \sin \phi \\ 0 \end{pmatrix} \quad (1.2)$$

Here, $\hbar\mathbf{k}_{\parallel}$ represents the component of the crystal momentum which is parallel to the surface. Due to lack of translational invariance perpendicular to the surface, the electron momentum component along this direction \mathbf{k}_{\perp} is not conserved. Because the system presented in this thesis is highly two-dimensional, the dependence of \mathbf{k}_{\perp} will not be treated further. More information can be found *e.g.* in [61].

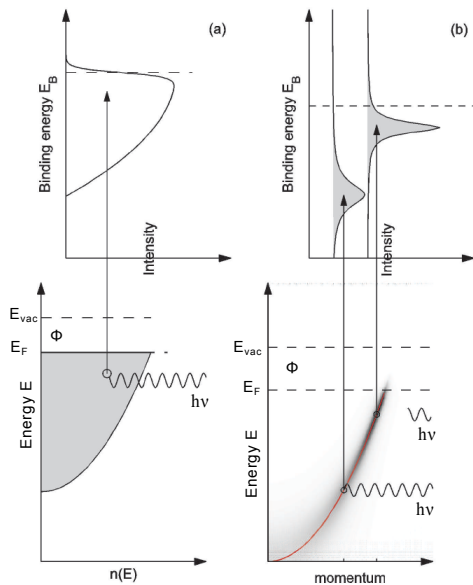


Figure 1.2: Energetics of the photoemission process within the single particle paradigm. **(a):** The density of states $n(E)$ is measured by angle integrated photoemissions spectroscopy. **(b):** Angle resolved photoemission spectroscopy is able to resolve the band structure, the electronic band dispersion. E_F denotes the Fermi level and is separated by Φ from the vacuum level E_{vac} . Adapted from [59].

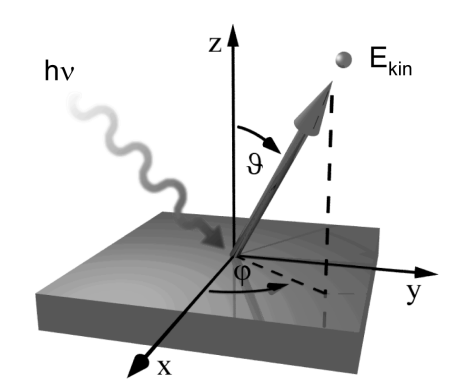


Figure 1.3: Schematic of the geometry of an ARPES experiment. The polar θ and azimuthal angle φ define the emission direction of the electron. Adapted from [60].

1.2 Scattering theory

To obtain a better understanding of the lowlying physics of the photoemission (PE) process and to describe correlations of the electronic system, the most important aspects of the PE process will be summarized in the following section. Describing the whole process in a rigorous quantum mechanical fashion would go far beyond the requirements to understand the basic physics behind the PE process. Anyway an analytic solution would only be possible with strong approximations.

Three step model:

Therefore the phenomenological *three-step* model [62], which has proven to describe the basic physics of the PE process will be summarized. The explicit steps, as illustrated in fig. 1.4, (a) are: (1) The electron absorbs a photon and is excited into a bulk final state. (2) The electron travels to the sample surface and (3) the electron escapes through the surface into the vacuum.

First step: The description of step (1) is simplified by invoking the concept of the *sudden approximation*: The excitation of one electron in the N -electron system is instantaneous and the electron is not interacting with the remaining $(N - 1)$ - electrons after the excitation. This assumption is justified for high kinetic-energy electrons (for photon energies as low as 20 eV). Therefore, the final state N -electron wavefunction Ψ_f^N of the system can be expressed in the same way as the initial state wave function Ψ_i^N . In the Hartree formalism Ψ_α^N ($\alpha = i, f$) is expressed as an antisymmetric product of a single-electron wave function $\phi_\alpha^{\mathbf{k}}$ and the remaining $(N - 1)$ -electron wave function Ψ_α^{N-1} :

$$\Psi_\alpha^N = \mathcal{A}\phi_\alpha^{\mathbf{k}}\Psi_\alpha^{N-1} \quad (1.3)$$

where the operator \mathcal{A} properly antisymmetrizes the whole wavefunction and $\alpha = i, f$ stands for the index of the initial state i or the final state f . The $(N - 1)$ -electron state is given by $\Psi_\alpha^{N-1} = c_{\mathbf{k}}\Psi_\alpha^N$ where $c_{\mathbf{k}}$ is the electron annihilation operator.

In first order perturbation, the transition probability w_{fi} between the N -electron initial state Ψ_i^N and the final excited state Ψ_f^N is described by *Fermi's golden rule*:

$$w_{fi} = \frac{2\pi}{\hbar} |\langle \Psi_f^N | V_{\text{int}} | \Psi_i^N \rangle|^2 \delta(E_f - E_i - h\nu) \quad (1.4)$$

where E_f and E_i are the initial and final-state energies of the N -particle system. The interacting potential V_{int} is given by [63]:

$$V_{\text{int}} = -\frac{e}{2mc} [\mathbf{p} \cdot \mathbf{A}(\mathbf{r}) + \mathbf{A}(\mathbf{r}) \cdot \mathbf{p}] + \frac{e^2}{2mc^2} |\mathbf{A}(\mathbf{r})|^2 \quad (1.5)$$

with \mathbf{A} being the electromagnetic vector potential of the incoming photon and \mathbf{p} the electronic momentum operator. In first order perturbation, the term $\propto |\mathbf{A}(\mathbf{r})|^2$ can be dropped. In the ultraviolet regime ($h\nu \gtrsim 3$ eV), \mathbf{A} is considered to be constant over atomic distances,

leading to $\nabla \cdot \mathbf{A} = 0$. Together with the comutator relation $[\mathbf{p}, \mathbf{A}] = i\hbar \nabla \cdot \mathbf{A}$, the interacting potential V_{int} can be written as:

$$V_{\text{int}} = \frac{e}{mc} \mathbf{A} \cdot \mathbf{p} \quad (1.6)$$

Because the interacting potential V_{int} just acts on the single electron state $\phi_i^{\mathbf{k}}$, the matrix element of equation 1.4 can be factorized into:

$$\langle \Psi_f^N | V_{\text{int}} | \Psi_i^N \rangle = \langle \phi_f^{\mathbf{k}} | V_{\text{int}} | \phi_i^{\mathbf{k}} \rangle \langle \Psi_f^{N-1} | \Psi_i^{N-1} \rangle \quad (1.7)$$

with the one-electron dipole matrix element $M_{f,i}^{\mathbf{k}} = \langle \psi_f^{\mathbf{k}} | V_{\text{int}} | \psi_i^{\mathbf{k}} \rangle$ and $\langle \Psi_f^{N-1} | \Psi_i^{N-1} \rangle$ being the $(N-1)$ -electron overlap integral. Decomposing the $(N-1)$ -electron state Ψ_f^{N-1} into eigenstates $\Psi_f^{N-1} = \sum_m \Psi_m^{N-1}$, with the eigenstate overlap $c_{m,i} = \langle \Psi_m^{N-1} | \Psi_i^{N-1} \rangle$, the total PE intensity $I(\mathbf{k}, E_{\text{kin}}) \propto \sum_{f,i} w_{f,i}$ is proportional to

$$\sum_{f,i,m} |M_{f,i}^{\mathbf{k}}|^2 |c_{m,i}|^2 \delta(E_{\text{kin}} + E_m^{N-1} - E_i^N - h\nu) \quad (1.8)$$

where the energy of the final state, Ψ_f^N , is given by the kinetic energy of the escaping electron, E_{kin} plus the sum of each eigenstate-energy:

$$E_f^N = E_{\text{kin}} + E_f^{N-1} = E_{\text{kin}} + \sum_m E_m^{N-1}. \quad (1.9)$$

In strong correlated electron systems (e.g. solids), many of the overlap integrals $c_{m,i}$ are different from zero. Therefore a rigorous solution of equation 1.8 will be complicated and unefficient. Rather, a slightly different expression for the PE intensity has been developed:

$$I(\mathbf{k}, E_{\text{kin}}) \propto \sum_{f,i} |M_{f,i}^{\mathbf{k}}|^2 A(\mathbf{k}, E) \quad (1.10)$$

where $A(\mathbf{k}, E) = A(\mathbf{k}, E)^+ + A(\mathbf{k}, E)^-$ is the so-called *one particle spectral function*. $A(\mathbf{k}, E)^+$ and $A(\mathbf{k}, E)^-$ can be interpreted as the one-electron addition or removal spectra. The spectral function is related to the single particle *Green's function*:

$$A(\mathbf{k}, E) = -\frac{1}{\pi} \text{Im} G(\mathbf{k}, E) \quad (1.11)$$

which is the sum of the one-electron addition and removal Green's function

$$G(\mathbf{k}, E) = G^+(\mathbf{k}, E) + [G^-(\mathbf{k}, E)]^* \quad (1.12)$$

These functions are defined as:

$$G^\pm(\mathbf{k}, E) = \sum_m \frac{|\langle \Psi_m^{N\pm 1} | \hat{c}_k^\pm | \Psi_i^N \rangle|^2}{E \mp (E_m^{N\pm 1} - E_i^N) \pm i\eta} \quad (1.13)$$

where \hat{c}_k^+ and \hat{c}_k^- are the electron creation (annihilation) operators. To account for electron-

electron interactions which play an important role in a strongly correlated system the energy gets renormalized by the *self energy* $\Sigma(\mathbf{k}, E) = \Sigma'(\mathbf{k}, E) + i\Sigma''(\mathbf{k}, E)$. The energy renormalization is contained in its real part $\Sigma'(\mathbf{k}, E)$ while the imaginary part, $\Sigma''(\mathbf{k}, E)$, describes the inverse electron lifetime. Including the correlations via $\Sigma(\mathbf{k}, E)$ into equations 1.12 and 1.11, the Green's- and spectral function are given by:

$$G(\mathbf{k}, E) = \frac{1}{E - \epsilon_k - \Sigma(\mathbf{k}, E)} \quad (1.14)$$

$$A(\mathbf{k}, E) = -\frac{1}{\pi} \frac{\Sigma''(\mathbf{k}, E)}{[E - \epsilon_k - \Sigma'(\mathbf{k}, E)]^2 + [\Sigma''(\mathbf{k}, E)]^2} \quad (1.15)$$

where ϵ_k is the bare band energy of the electron. By applying these considerations, the total ARPES intensity can be expressed as:

$$I(\mathbf{k}, E) = I_0(\mathbf{k}, \nu, \mathbf{A})f(E)A(\mathbf{k}, E) \quad (1.16)$$

with $I_0(\mathbf{k}, \nu, \mathbf{A}) \propto |M_{f,i}^{\mathbf{k}}|^2$ and $f(E) = (e^{(E-E_F)/k_B T} + 1)^{-1}$ denoting the Fermi distribution which takes into account that photoemission only probes occupied states.

Second step: Coming back to the three-step model, the second step describes the travel of the electron to the crystal surface. The photoexcited electron mainly interacts via inelastic electro-electron scattering on its way to the surface. By assuming an isotropic scattering rate, the inelastic mean free path only depends on the energy of the electron and is described by the so called *universal curve*, presented in fig. 1.5. The energy range of the SIS beamline is indicated by the shaded region. This curve is called universal because the escape depth of the electron is roughly material independent. Inelastic scattering processes of electrons on the way to the surface form the intrinsic background which is usually ignored or subtracted. **Third step:** Step number (3) describes with the escape of the electron through the crystal surface. To escape the crystal the electron has to overcome the surface potential barrier ϕ . Therefore the escape probability depends on the energy of the electron and the material work function ϕ .

As mentioned in the beginning of this section, the three step model is purely phenomenological but has proven to describe the lowlying physical properties of the PE process successfully. To subdivide the whole process into three independent steps, relevant simplifications have to be done. The strongest approximations are: The interference of the bulk outgoing state and surface emitted state are neglected. The model also doesn't account for interference of scattered and unscattered waves during their way to the surface. The escaping process is very simplified and only described by a single parameter. A correct treatment of the PE process is given by the so called *one - step* model which is illustrated in fig. 1.4. The excitation is based on Fermi's golden rule which is presented in equation 1.4 and uses the proper wave functions for the initial and final state. All the physics is contained in the dipole operator for the electron-phonon interaction. Unfortunately the problem cannot be

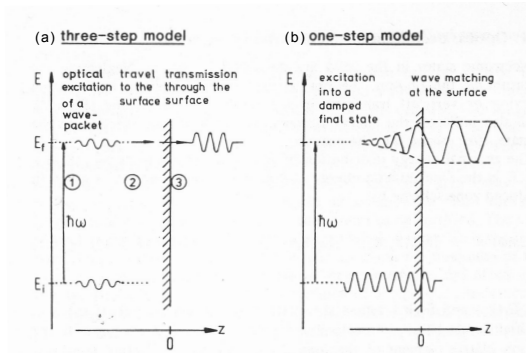


Figure 1.4: (a): Schematic of the three-step model: (1) Escitation of the electron by the photon. (2) travel of the electron to the surface (3) transmission through the surface into the vacuum. (b): One-step model: Bloch wave electron is excited and described as a free wave in vacuum which is decaying in the solid. Taken from [61]

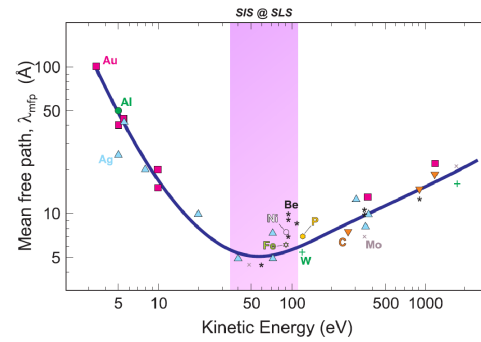


Figure 1.5: Universal curve of the photoelectron escape depth for various materials. The shaded region is representing the usual energy range of the SIS beamline at PSI. Taken from [64]

solved rigorously without employing various approximations. A succesfull approximation is given by the inverse LEED final state, presented *e.g.* in the book of Hüfner *et al.* [61]. A complete treatment of the whole formalism invoked in one-step calculation would surely go beyond this work. Further information and extensive treatment can be found in [61, 63, 65].

Chapter 2

Experimental Methods: Measurement setup - sample preparation

2.1 Experimental setup - ARPES applied

The ARPES measurements were done at the ARPES end station of the SIS beam line at PSI, Villigen (CH) using a high resolution photo emission analyzer Scienta R4000. A schematic of an ARPES beamline at a synchrotron facility is presented in figure 2.1. The advantage of synchrotron light compared to gas-discharge lamps (for example He-lamps) and laser sources is given by the availability of wide energy range of intense and highly polarized light. The beam of white light is produced by the undulator, see fig. 2.1. In synchrotron facilities, these ‘insertion devices’ appear as straight lines in the circle of the electron beam. To select the appropriate wavelength of the light, the white light is monochromated by a grating monochromator. After the light was focused on the sample, the emitted electrons travel through the electron-lens system into the analyzer where an electric field is applied between the inner and outer concentric spheres. Deflected by the electric field, electrons with different kinetic energies travel on a half-circle with different radii to the detector. Electrons with higher kinetic energy are deflected less and therefore hit the detector at a bigger radius than low-kinetic energy electrons do. Now, the electrons are energy resolved according to the detector-radial axis. The tangential component of the 2 dimensional detector describes the momentum of the electron. Modern detectors commonly use a CCD camera to detect the electrons. According to the detector datasheet, provided by the company [66], the angular resolution is 0.4 for a 1 mm emission spot on the sample. The energy resolution during our measurements was approximately 19 meV in a temperature region of $T \approx 12 - 22$ K. Due to matrix element effects the measurements were done mainly in the second Brillouin zone with circular polarized light of 55 eV.

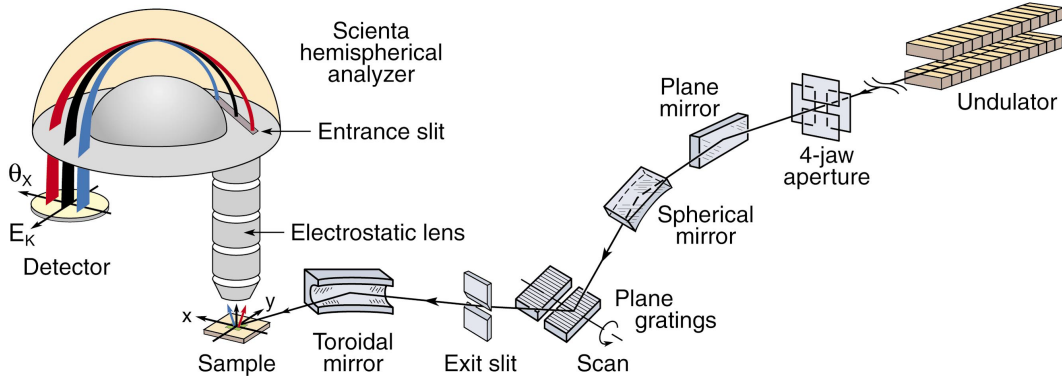


Figure 2.1: Schematic of an ARPES beamline of a synchrotron source. As detector a hemispherical analyzer is used. Adapted from [2].

2.2 Cuprate Compounds

2.2.1 Crystal structure

In this chapter, the basic crystal properties of the high temperature superconductor (HTSC) $\text{La}_{1.6-x}\text{Sr}_x\text{Nd}_{1.6}\text{CuO}_4$ (Nd-LSCO) will be discussed. In this material Lanthanum atoms were replaced by a fixed amount of Neodymium and a variable amount of Strontium. Strontium has one valence electron less than La and therefore the amount of chemical doping (indicated by x) directly gives the amount of holes doped into the system (indicated by p). The crystal structure which is presented in figure 2.2 consists of a pile of alternating LaO and CuO_2 layers which show weak interlayer coupling. This makes the system highly two dimensional and therefore preferential for ARPES (see section 1.1). The weak interlayer coupling also allowed us to cleave the samples *in situ* to obtain a clean and flat surface. For temperatures below $T \lesssim 70$ K the crystal is in the so called low temperature tetragonal phase (LTT) [19]. In the LTT phase, the lattice constant along direction a and b (see fig. 2.2) are equal $a = b = 3.78 \text{ \AA}$. The lattice constant along the c -direction is $c = 13.18 \text{ \AA}$. A phase diagram for this compound, based on resistivity measurements is presented in fig: 1.1.

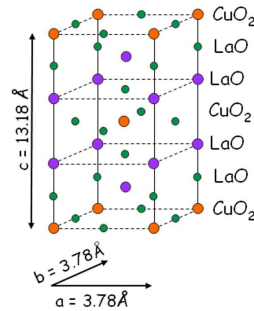


Figure 2.2: Ordering of the individual layers in a pure LaCuO_4 crystal. La - atoms are replaced by Sr and Nd in our crystal. Taken from [67].

2.2.2 Sample preparation

Ex-situ preparation:

The samples were grown by the group of J.B. Goodenough at Texas Materials Institute (TMI) using the traveling-float-zone technique (TFZT). The doping of each crystal was determined by R. Daou *et al.* from its T_c and $\rho(250\text{K})$ values compared to published data [4]. The crystals were aligned by use of a Laue X-ray diffractometer operated with a tube current of 40 mA and a voltage of 40 kV. A typical Laue pattern with the X-ray beam pointing along the crystal c-axis is presented in fig. 2.4. The angles α and β are not equal and therefore a clear orientation of axis a and b is possible. The axis orientation is labeled in figure 2.4. After orienting the crystal, a wire saw (tungsten wire) was used to cut the crystal. Cutting these comparatively hard crystals with the wire saw took a large amount of time (several hours), but minimized the wastage of sample because of the real thin tungsten wire (≈ 0.1 mm). After the samples had been cleaned with Aceton, they were glued with conducting silver epoxy ¹ on specific copper sample holders which suite the *CARVING* ² manipulator of the ARPES machine (see fig.2.3). By use of non conductive Torr seal ³, an aluminium pin was glued on top of the sample and a small wireloop on top of the pin. After glueing the whole setup was put for several hours on a heating plate (80° C).

In situ preparation:

Before cleaving the sample, the sample holder was sputtered for approximately 30 min with argon gas to clean some part of the sample holder (pressure inside the sputtering chamber stayed below 10^{-6} Torr). The gun controll settings ⁴ were 10 mA and 1000 V. This allowed us to record a copper spectrum for the purpose of determining the Fermi level (the exact procedure of the Fermi calibration will be explained in one of the following sections). In order to avoid an artificial shift of the Fermi level of the sample surface with respect to the copper sample holder it was very important that the sample surface was in good electrical contact with the sampleholder.

After the sample had been mounted on the manipulator and cooled to base temperature, it was cleaved in UHV ($\lesssim 5 \cdot 10^{-11}$ Torr). The cleaving process guaranteed to obtain an ultra clean surface of the sample, essential for successful ARPES measurements. The loop on the pin helped to recover the pin together with the part of the sample which was sticking on it. The recovering of the pin was done with aid of a specially designed pin can which was in principle a usual sampleholder with a large hole drilled inside.

¹Polyscience AG, EPO-TEK E 411

²CARVING: (Complete Angle Resolved Variation for electron spectroscopy IN VilliGen) is the name of the current manipulator installed at the Surface and Interface Spectroscopy (SIS) beamline at Paul Scherrer Institute, Switzerland

³Torr Seal Resin Sealant, Agilent Technologies. Special sealant for UHV applications. Is harder then silver epoxy.

⁴Commercial system, Omicron ISE 10 Sputter Ion Source

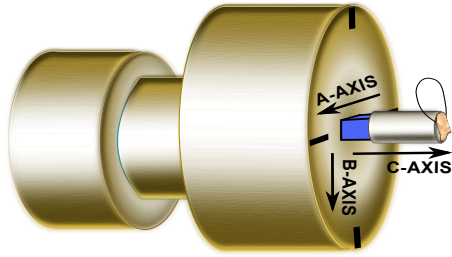


Figure 2.3: Shape of the usual ARPES sampleholder, suitable for the CARVING manipulator at SIS beamline. The sample (blue) was glued with conducting silver epoxy. A pin was glued on top of the sample by Torr seal in order to cleave *in situ*. The loop helped to handle the pin after cleaving. The marker on the sampleholder indicated the direction of A and B axis.

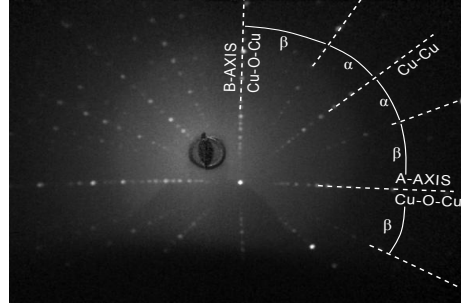


Figure 2.4: Typical Laue diffraction pattern of a Nd-LSCO single crystal measured with 40 mA and 40 kV with the X-ray beam along the c-axis. The diffraction shows a four fold symmetry. The fact that α is not equal to β allows to orient the crystal.

2.3 Calibration and Normalization of ARPES spectra

In this section a first, brief introduction of ARPES spectra is presented and one possible way of determining the Fermi level and normalizing the ARPES spectra is shown. Figure 2.5, (a) shows a raw ARPES spectrum, a colorcoded intensity map as function of energy and detector angle (detector channel), of polycrystalline copper. By analyzing the spectrum, a significant step of intensity at a kinetic energy of ≈ 50.65 eV and a modulation of energy integrated spectral weight at different angles (detector channels) can be observed. In order to do a first step of analysis, we go back to the theoretical prediction for an ARPES spectrum of section 1.2: $I(\mathbf{k}, E) = I_0(\mathbf{k}, \nu, \mathbf{A})f(E)A(\mathbf{k}, E)$. In the vicinity of the Fermi level E_F , the spectral function $A(\mathbf{k}, E)$ and the Matrix element which is proportional to $I_0(\mathbf{k}, \nu, \mathbf{A})$ is assumed to vary only slightly as function of energy. Because the copper is polycrystalline with random orientation of the individual microscopic crystals, the intensity is independent of \mathbf{k} . Comparing the observation of the spectrum with these considerations on energy and momentum dependence, the following conclusions can be drawn: The most significant step of the ARPES intensity is due to the Fermi distribution (FD) $f(E) = [1 + e^{(E-E_F)/k_B T}]^{-1}$ and therefore can unambiguously be associated with the drop of intensity at 60.65 eV. A constant momentum cut as indicated by the white dashed line in panel (a) is presented for the energy region around E_F in panel (c). To determine the detector channel dependent value of the Fermi level $E_F(n)$ (n indicating the detector channel), the measurement is fitted by the FD function $f(E)$. A momentum independent value of the Fermi level is obtained by transforming the kinetic energy into the binding energy for each detector channel n :

$$-E_B = E_{\text{kin}} - E_F(n) \quad (2.1)$$

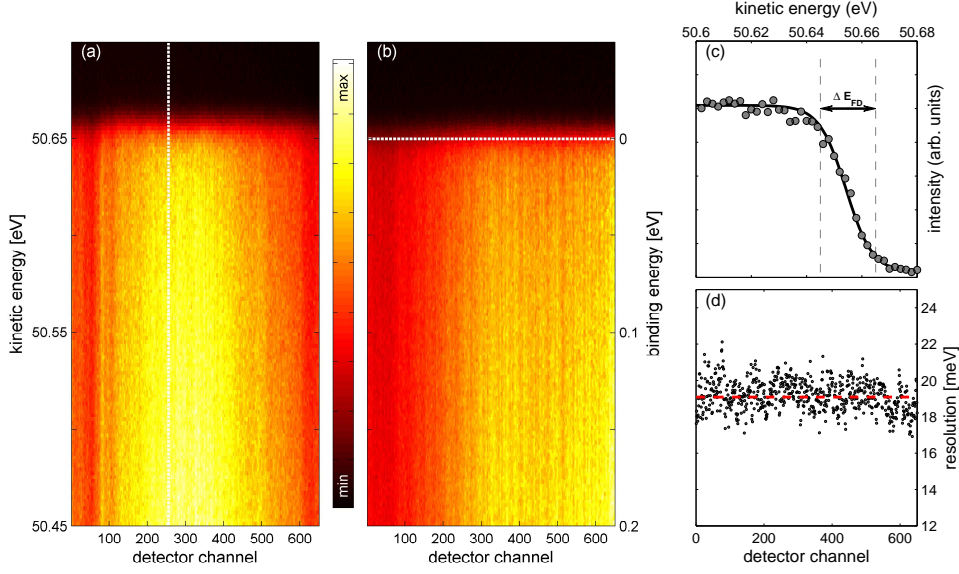


Figure 2.5: (a): Raw, unmodified ARPES spectrum of polycrystalline copper of the Ar-sputtered sampleholder at $T = 22$ K. The significant intensity step is interpreted as the Fermi level. The Fermi level and the overall intensity vary for each detector channel. (b): Calibrated polycrystalline copper spectrum (panel (a)) according to equation 2.1. Each detector channel intensity is normalized with respect to the intensity above the Fermi level. (c): Intensity distribution *vs.* kinetic energy of the electrons at the cut indicated by the white dashed line in panel (a). ΔE_{FD} denotes the total energy resolution in the 12%-88% criterion. The data is fitted by the Fermi distribution function. (d): This figure presents the resolution for each channel extracted by the method which is shown in panel (c). The average resolution is shown by the red line.

Secondly the strong variation of intensity for different momenta is explained by different detector channel efficiencies. Therefore, for each measurement, the intensity of each detector channel is normalized by background spectral weight above E_F ⁵. The calibrated and normalized spectrum of the one presented in panel (a) is plotted in (b). From now on, each spectrum was calibrated with respect to the fermi level in polycrystalline copper and normalized with respect to its own background intensity. The total energy resolution of the experiment was determined by the broadening of the Fermi edge. In this report, the total energy resolution is given by $\Delta E_{tot} = 4k_B T$ what is the energy range between 12% and 88% of the maximum as indicated in panel (c). ΔE_{tot} for each channel n is indicated in panel (d). The average is illustrated by the red line. During the whole experiment the energy resolution was around 17-19 meV for base temperatures (12-22) K and approximately 30 meV for $T = 80$ K.

⁵Due to thermal broadening, only states far above $E_F + 2k_B T$ should contribute to the normalizing factor.

2.4 Analyzing ARPES data

2.4.1 MDC and EDC method

In the preceding section a usual ARPES spectrum was presented as an 2D-intensity plot as function of binding energy E_B and momentum (fig.2.5, (b)). To extract all the information which is contained in these spectra several ways of analysis will be discussed. A very basic way of presenting ARPES data is given by either plotting momentum distribution curves (MDC) i.e. intensity versus momentum for a given binding energy (fig. 2.6, (b)) or plotting an energy distribution curve (EDC) at a given momentum (fig. 2.6, (c)). If we assume slowly varying Matrix elements and momentum independence of the self energy ($\partial\Sigma/\partial k \approx 0$), the MDC lineshape which is then entirely described by $A(\mathbf{k}, E)$ is Lorentzian like ⁶ [59].

$$A(\mathbf{k}, E) = -\frac{1}{\pi} \frac{\Sigma''(E)}{[E - \epsilon_k - \Sigma'(E)]^2 + [\Sigma''(E)]^2} \quad (2.2)$$

Kaminski *et al.* [68] found in a systematic study that the background of the MDC is purely extrinsic and can be described by:

$$I_{\text{MDC}}(k) = a + bk \quad (2.3)$$

where a and b are constant and k denotes the momentum. Due to the extrinsic nature of the background, the total ARPES intensity can be written as the sum of the intrinsic contribution $I_{\text{int}}(\mathbf{k}, E)$ and the extrinsic background $I_{\text{bg}}(\mathbf{k}, E)$:

$$I(\mathbf{k}, E) = I_{\text{int}}(\mathbf{k}, E) + I_{\text{bg}}(\mathbf{k}, E) \quad (2.4)$$

$$= I_0(\mathbf{k}, \nu, \mathbf{A})f(E)A(\mathbf{k}, E) + I_0^{bg}(\mathbf{k}, \nu, \mathbf{A})f(E)B(\mathbf{k}, E) \quad (2.5)$$

Where the matrixelement containing function $I_0^{bg}(\mathbf{k}, \nu, \mathbf{A})$ depends differently on the photon energy and \mathbf{k} than $I_0(\mathbf{k}, \nu, \mathbf{A})$. The fitted Lorentzian (black curve) is overlaid on the MDC (red dots) in panel (b). Because the spectral function which is given in equation 2.2 is highly energy dependent and the FD function gives another additional step in the ARPES spectrum, the EDC can not be described by such a simple lineshape.

Fortunately, to simplify the lineshape of the EDC, a method exists to get rid of the big effects in the vicinity of E_F caused by the FD function. For a quantitative gap analysis which takes place in the direct region around E_F this is a very helpful achievement. By assuming particle hole symmetry, the EDC can be *symmetrized* with respect to $E_F = 0$ eV by reflecting the EDC at $E_F = 0$ eV and summing up the original and reflected EDC:

⁶Broadening by finite momentum resolution as negligible

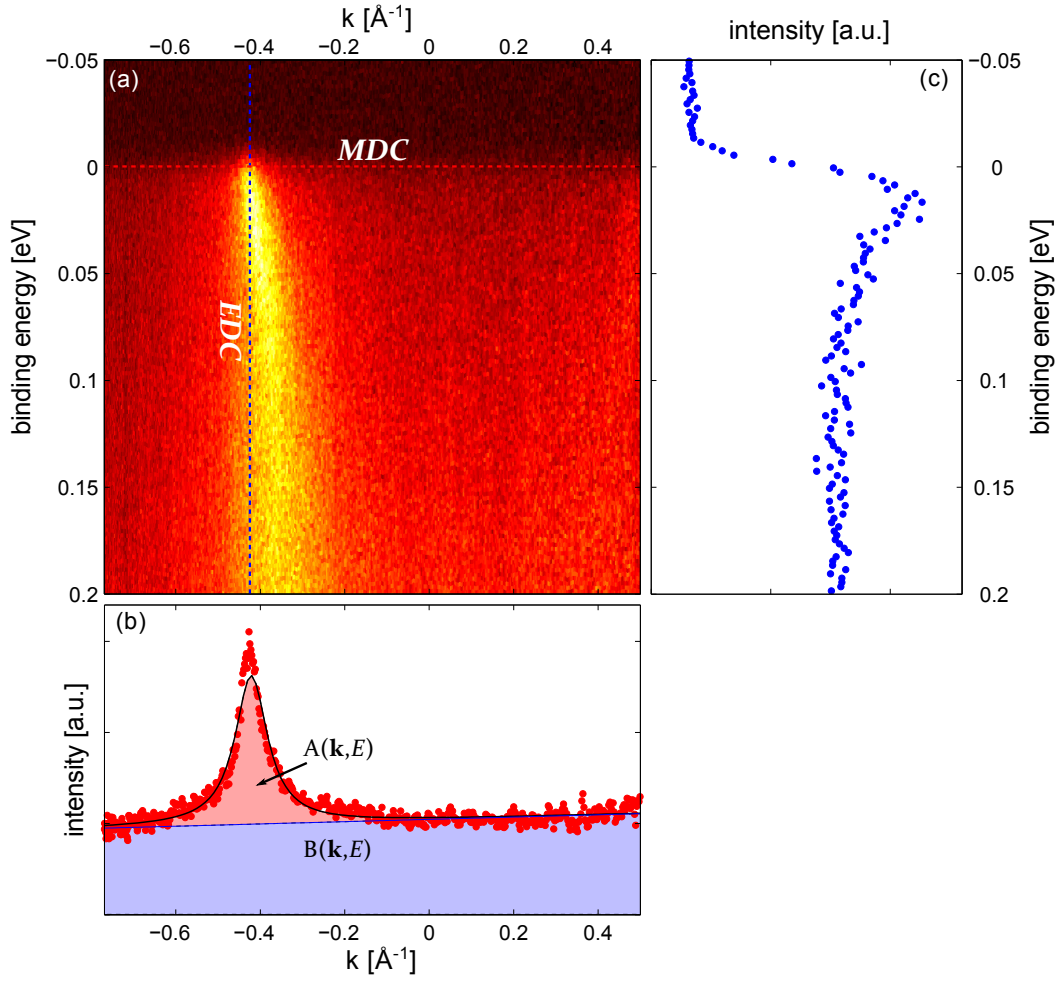


Figure 2.6: (a):ARPES intensity map showing a part of the band dispersion of Nd-LSCO $x = 0.20$ as function of the binding energy and momentum \mathbf{k} . The horizontal red dashed line indicate the position of the momentum distribution curve (MDC) presented in (b) and the blue curve the position of the energy distribution curve (EDC) shown in (c). The blue shaded area in (b) indicates extrinsic background ($\propto B(\mathbf{k}, E)$) where the red region marks intensity described by the spectral function $A(\mathbf{k}, E)$. The MDC is fitted by a Lorentzian. The EDC cannot be described by such a simple lineshape.

$$\begin{aligned}
I_{\text{sym}}(\mathbf{k}, E) = I(\mathbf{k}, E) + I(\mathbf{k}, -E) &= I_0(\mathbf{k})f(E)A(\mathbf{k}, E) + I_0(\mathbf{k})f(-E)A(\mathbf{k}, -E) \\
&= I_0(\mathbf{k})f(E)A(\mathbf{k}, E) + I_0(\mathbf{k})[1 - f(E)]A(\mathbf{k}, E) \\
&= I_0(\mathbf{k})A(\mathbf{k}, E)
\end{aligned} \tag{2.6}$$

Here, the identity $f(-E) = 1 - f(E)$ was used and the particle hole symmetry of the system is contained in $A(\mathbf{k}, E) = A(\mathbf{k}, -E)$. This method was commonly used for cuprates [28, 44, 52, 37]. To extract the gap value, a phenomenological self energy function Σ which is based on the BCS self energy and modified for the pseudogap state was proposed by Norman *et al.* [37].

$$\Sigma(\mathbf{k}, E) = -i\Gamma_1 + \frac{\Delta^2}{E + \epsilon_{\mathbf{k}} + i\Gamma_0} \tag{2.7}$$

Where Γ_0 was interpreted to be the inverse pair lifetime which is infinite below T_c . Γ_1 is the single particle scattering rate and Δ the gap size. The symmetrizing process is visualized in fig. 2.7, (a) for Nd-LSCO, $x = 0.20$ in the antinodal region around $(1,0)^7$ (upper curve) where the pseudogap is open and in the nodal region around $(1/2, 1/2)$ (lower curve) where the spectrum is ungapped. To account for the energy resolution, the raw intensity had to be convolved with the finite energy resolution of the setup. The resolution function $\mathcal{R}(E)$ was usually given by a Gaussian with the FWHM representing the total energy resolution ΔE_{tot} .

$$I_{\text{sym}}(\mathbf{k}, E) = I_0(\mathbf{k})A(\mathbf{k}, E) \otimes \mathcal{R}(E) \tag{2.8}$$

Panel (b) shows again the symmetrized data of panel (a) in form of open circles with the fit on top. In the case of the ungapped spectrum (bottom), the spectral function, $A(\mathbf{k}, E)$, was assumed to be Lorentzian and thus the convolution with the Gaussian resolution is called a Voigt profile.

⁷The units are given in $\frac{\pi}{a} \text{ \AA}^{-1}$ with the lattice constant $a = 3.78 \text{ \AA}$.

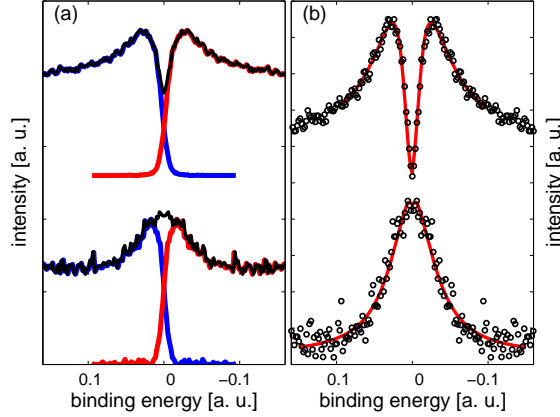


Figure 2.7: (a): *Blue*: EDCs of Nd-LSCO $x = 0.20$ in the antinode (AN), (top curve) in the node (N), (bottom curve). *Red*: EDCs reflected at $E = 0$ eV. *Black*: Sum of the original and reflected EDCs (symmetrized EDC). (b): Symmetrized EDCs of (a) are fitted with a resolution broadened Lorentzian (Voigt) curve (bottom red curve) and a gapped, resolution broadened Lorentzian function [37].

2.4.2 Conversion from detector angles into k-space

To study a wide range of the reciprocal space by ARPES with cuts along different orientations, the ARPES endstation provides the *CARVING* manipulator with rotational freedom around three axes. A schematic (fig. 2.8) illustrates the setup of the axes. The intrinsic manipulator coordinate system (blue) x', y', z' is oriented along the high symmetry lines of the sample with x' and y' along a and b and z' along the c -axis of the sample. If all manipulator angles are set to zero, the intrinsic coordinate system is equal to the laboratory system which is indicated by the red lines x, y, z . In the laboratory system, the analyzer slit lies in the x - z plane.⁸ The rotations of the manipulator are described by the angles Θ (around Y), χ (around the new axis X')⁹ and Φ (around the new axis Z'). Note, that α denotes a rotation around the same axis as Θ (y -axis). As we saw already in equation 1.2, the absolute value of the momentum-component

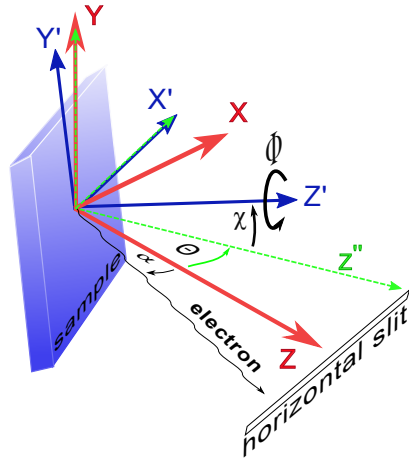


Figure 2.8: Sketch of the ARPES angles available at the *CARVING* manipulator.

⁸This is valid for horizontal slit setting. For vertical setting, the analyzer slit is parallel to y and perpendicular to x and z . The transformation would be basically the same.

⁹At SIS beamline, this angle is called *tilt*.

which is parallel to the surface is given by: $p_{||} = \sqrt{2mE_{\text{kin}}} \sin \vartheta$. The angle ϑ can be directly connected with the detector angle α . The crystal momentum $\mathbf{k} = \mathbf{p}/\hbar$ of the electron in the laboratory system is therefore given by:

$$\mathbf{k} = \frac{\sqrt{2mE_{\text{kin}}}}{\hbar} \begin{pmatrix} -\sin \alpha \\ 0 \\ \cos \alpha \end{pmatrix} \quad (2.9)$$

In order to transform the components of this vector into the crystal coordinate system, we use the following rotation matrices:

$$R_{\Theta} = \begin{pmatrix} \cos \Theta & 0 & -\sin \Theta \\ 0 & 1 & 0 \\ \sin \Theta & 0 & \cos \Theta \end{pmatrix}, R_{\chi} = \begin{pmatrix} 1 & 0 & 0 \\ 0 & \cos \chi & \sin \chi \\ 0 & -\sin \chi & \cos \chi \end{pmatrix}, R_{\Phi} = \begin{pmatrix} \cos \Phi & -\sin \Phi & 0 \\ \sin \Phi & \cos \Phi & 0 \\ 0 & 0 & 1 \end{pmatrix} \quad (2.10)$$

The momentum in the crystal coordinate system, \mathbf{k}' , is consequently given by:

$$\mathbf{k}' = R_{\Phi} R_{\chi} R_{\Theta} \mathbf{k} \quad (2.11)$$

So far we assumed, that the crystal axes a, b and c are perfectly aligned with the axes of the manipulator. In real ARPES experiment, this is rarely achieved and therefore has to be corrected by the following correlation. The mismatching angle between the crystal c -axis and the manipulator z' -axis will be considered as γ and β denotes the angle between the a -axis and manipulator x' -axis. The resulting crystal momentum is then given by:

$$\mathbf{k}' = \begin{pmatrix} \cos \beta & -\sin \beta & 0 \\ \sin \beta & \cos \beta & 0 \\ 0 & 0 & 1 \end{pmatrix} \begin{pmatrix} \cos \gamma & 0 & -\sin \gamma \\ 0 & 1 & 0 \\ \sin \gamma & 0 & \cos \gamma \end{pmatrix} \begin{pmatrix} \cos \beta & \sin \beta & 0 \\ -\sin \beta & \cos \beta & 0 \\ 0 & 0 & 1 \end{pmatrix} R_{\Phi} R_{\chi} R_{\Theta} \mathbf{k} \quad (2.12)$$

Chapter 3

The Fermi surface of Nd-LSCO

Having introduced all relevant aspects of angular resolved photoemission spectroscopy (ARPES), sample preparation and basic characteristics of the high temperature superconductor (HTSC) compound $\text{La}_{1.6-x}\text{Sr}_x\text{Nd}_{0.4}\text{CuO}_4$ (Nd-LSCO) we now turn to the results. In this chapter the evolution of the Fermi surface as function of doping will be presented.

3.1 Evolution of the Fermi surface - Introduction

The concept of the Fermi surface (FS) is playing an important role in the field of condensed matter physics. In metallic material, filled and unfilled states in the reciprocal space (k -space) are separated by the locus of points which describe gapless electronic excitations, called the Fermi surface. To obtain new insights on the mechanism of HTSCs, major efforts were done to resolve and understand the doping dependence of low-energy excitations near the FS. For example on high T_c cuprates an amazing amount of research was done to reveal the correct size and shape of the FS. In order to get a direct probe of the FS of a material, ARPES and quantum oscillations (QO) are among the best techniques.

On the overdoped side, there is common agreement that the FS is rather large and centered around (0,0) (Γ) or (1,1) in reciprocal space. This is seen *e.g.* by QO on $\text{Ti}_2\text{Ba}_2\text{CuO}_{6+\delta}$ (Ti2201) [6] or ARPES on Ti2201 and LSCO [7, 9] and is supported by LDA calculations [8]. The large electronlike Fermi surface satisfies the Luttinger theorem [10] which states that the Fermi surface is unchanged in presence of weak interactions. In this picture, the FS area is scaling with the electron density $n = 1 - p$. Where p is the hole doping concentration per Cu.

Inside the pseudogap phase the low energy excitation particles are ‘gapped out’ in the region around (1,0) (antinode) and ‘survive’ only as so called ‘Fermi arcs’ around (1/2,1/2) (nodal region). On the underdoped side, concerning the Fermi surface, two scenarios exist and are supported by different experiments. Quantum oscillation experiments in underdoped $\text{YBa}_2\text{Cu}_3\text{O}_{6.5}$ (YBCO) reveal the existence of a Fermi surface made of at least one small pocket [11, 12]. This suggests a Fermi surface reconstruction by charge and spin ordering

phase states (‘sripe’ state) in these material [15, 16].

In contrast, ARPES experiments observe the above mentioned Fermi arcs [42, 17, 43].

A common procedure in ARPES experiments is to investigate the ‘underlying’ Fermi surface. One possible way to determine the ‘underlying’ Fermi momenta \mathbf{k}_F is given by the so called ‘MDC-method’ which is described in the following section and in works of Yoshida *et al.* [9] or Shen, K.M. *et al.* [17]. In underdoped LSCO, Yoshida *et al.* [9] found a large underlying Fermi surface. The enclosed area was in good agreement with the expectations by electron count $n = 1 - p$ while experiments on $\text{Ca}_{2-x}\text{Na}_x\text{CuO}_2\text{Cl}_2$ $\text{Ca}_{2-x}\text{Na}_x\text{CuO}_2\text{Cl}_2$ (Na-CCOC) [17] revealed significantly larger Fermi surfaces as predicted by the Luttinger theorem.

In this chapter, the evolution of the underlying Fermi surface in the normal state ($T_c < T < T^*$) of Nd-LSCO ($\text{La}_{1.6-x}\text{Sr}_x\text{Nd}_{0.4}\text{CuO}_4$) within a wide doping range $x = 0.15, 0.20$ and 0.24 is presented in a systematic ARPES study. The results will be compared to former ARPES studies on other hole doped cuprates.

3.2 The FS of Nd-LSCO

3.2.1 Results

The measured Fermi surface of Nd-LSCO, $x = 0.15, 0.20$ and 0.24 is presented in spectral intensity maps in k -space in figure 3.1, a)-c). The spectral weight was integrated around E_F in a region of ± 10 meV and normalized to background intensity above E_F of each EDC (described in section 2.3). By fitting a Lorentzian curve to the energy-integrated momentum distribution curve (MDC) at E_F , the Fermi momentum \mathbf{k}_F could be identified by the peak position of the fit (MDC-method). The resulting \mathbf{k}_F are indicated as white dots in figure 3.1, a)-c). It was shown by Borisenko *et al.* [18] that the error by determining \mathbf{k}_F with this method is very small for ungapped systems and also can be applied if a gap opens in the electronic excitation spectrum at the Fermi level. If the pseudogap opens in the antinodal region, spectral weight is suppressed at the Fermi level. However, the suppression is only partial and therefore states near the Fermi level are sufficiently occupied to determine the underlying Fermi momenta \mathbf{k}_F .

A first implication which could be drawn by analyzing the extracted \mathbf{k}_F is the following: For the doping value $x = 0.15$ the Fermi surface is clearly hole like and centered around the Y point at (1,1). By contrast, the Fermi surface for $x = 0.24$ is electron like and centered around Γ . For $x = 0.20$ the positions of extracted \mathbf{k}_F values indicate a hole like FS. However a cut at (1,0) as indicated in the inset of figure 3.2, a) suggests an electron like FS. The intensity distribution shows a peak at $k_y = -1.2 \frac{\pi}{a}$ on one side of the Brillouin zone (BZ) boundary and a shoulder at $k_y = -0.9 \frac{\pi}{a}$ on the other side (in the first BZ). The shoulder could be interpreted as a peak of similar shape which is strongly suppressed by small matrix elements in the first BZ [20]. Two peaks on both sides of the BZ-boundary would unambiguously lead to the conclusion, that the Fermi surface is electron like. To draw a clear

conclusion on that issue, further investigations in this region of the BZ have to be done in future experiments.

3.2.2 Analysis of the FS

For temperatures below $T \approx 60$ K the system is in low temperature tetragonal (LTT) phase [19]. Therefore the Fermi momenta were symmetrized according to tetragonal symmetry and visualized by blue dots in figures 3.1, e) - h).

A tight binding fit of the extracted values of \mathbf{k}_F according to equation 3.1 is shown by green lines in figures 3.1 a) - d) and by black lines in figures e) - h).

$$\begin{aligned} \varepsilon_k = \varepsilon_0 - 2t[\cos(k_x a) + \cos(k_y a)] - 4t'(\cos(k_x a) \cos(k_y a)) - 2t''[\cos(2k_x a) + \cos(2k_y a)] \\ - 4t'''[\cos(2k_x a) \cos(k_y a) + \cos(k_x a) \cos(2k_y a)] - 4t'''' \cos(2k_x a) \cos(2k_y a) \end{aligned} \quad (3.1)$$

The parameters t, t', t'', t''', t'''' are the first-, second-, third-, fourth-, and fifth nearest neighbor hopping parameters between Cu sites. The ratios with respect to t are presented in table 3.1.

	x_{FS}	ε_0/t	t'/t	t''/t	t'''/t	t''''/t
p = 0.15	0.247	1.2180	-0.3097	0.001	-0.01	0.02
p = 0.20	0.268	1.2377	-0.3182	-0.0025	0	-0.001
p = 0.24	0.29	1.0682	-0.2319	0.004	0.01	0.02

Table 3.1: Fermi surface area and tight binding fitting parameters of equation 3.1) as shown by green/black lines in 3.1, a) - d)/e) - h).

The FS which is now described by this tight-binding model separates the occupied (shaded region in fig. 3.2) from the unoccupied part in the BZ. The hole number x_{FS} , as deduced by the area of the shaded region of panel e) - h) is plotted in figure 3.2, b) against the expectation by Luttinger's theorem (dashed black line) and measurements on LSCO [9] and Na-CCOC [17]. As the figure shows, on the overdoped side, LSCO tends to have a slightly smaller ¹ FS area than in uncorrelated systems. Towards the underdoped side the FS area of LSCO and Na-CCOC is larger implying smaller (even negative) hole counts. Compared to these former ARPES studies on LSCO [9] the volume of the underlying Fermi surface follows a similar behavior and satisfies Luttinger's theorem within the error bars for the whole. The Fermi surface volume $x_{FS} \approx 0.12$ for $x = 0.12$ is taken from former studies by Chang *et al.* [14]. Measured data is in contrast to studies on Na-CCOC [17] and

¹Here we are using the nomenclature of Yoshida *et al.*, [9]. A smaller electron like FS results in larger hole count.

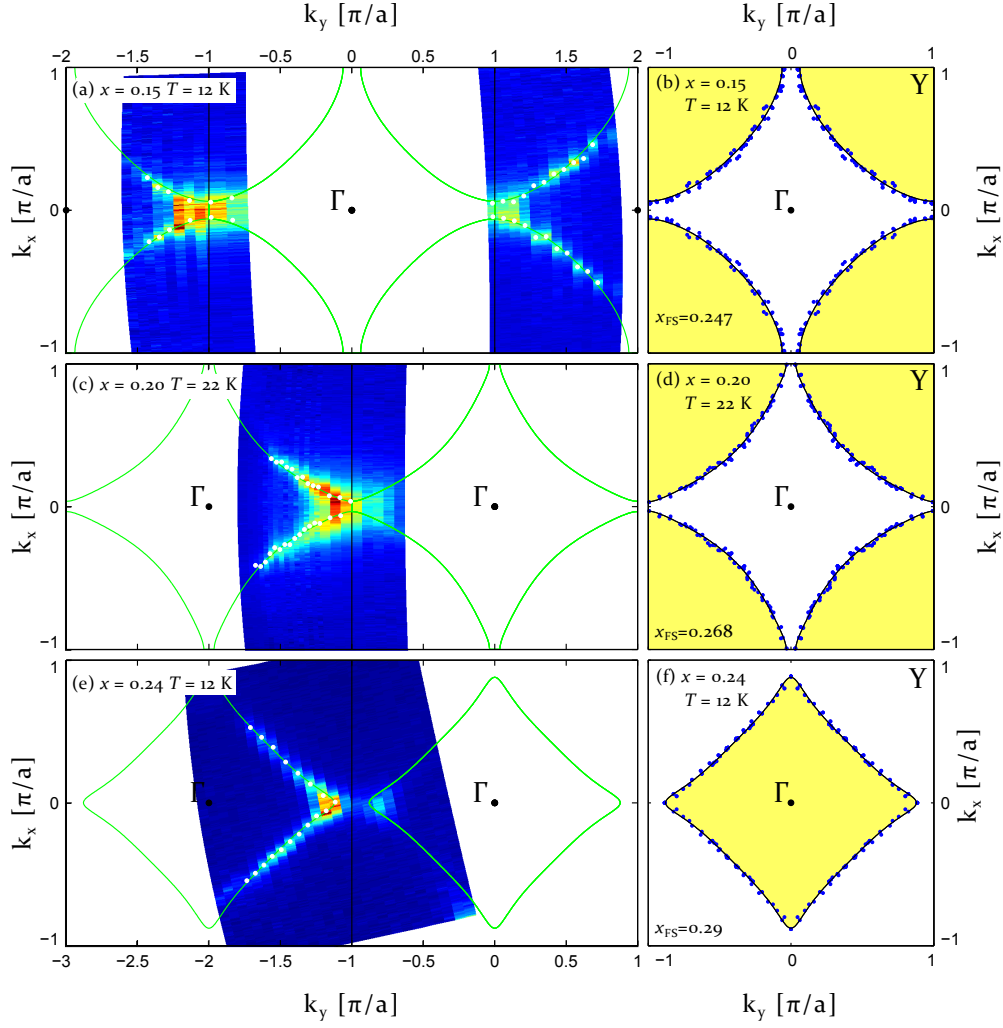


Figure 3.1: (a),(c),(e): Intensity maps in k space of the Nd-LSCO Fermi surface (spectral weight at E_F , integrated over ± 10 meV). White circles indicate the position of \mathbf{k}_F determined by the MDC maximum at E_F . Green lines indicate a fit by the tight binding model, (see equation: 3.1). (b),(d),(e): The values of \mathbf{k}_F , indicated as white circles in (a) - (d) are folded into the first BZ and symmetrized according to the tetragonal crystal structure. The Fermi surface area x_{FS} is indicated by the shaded area.

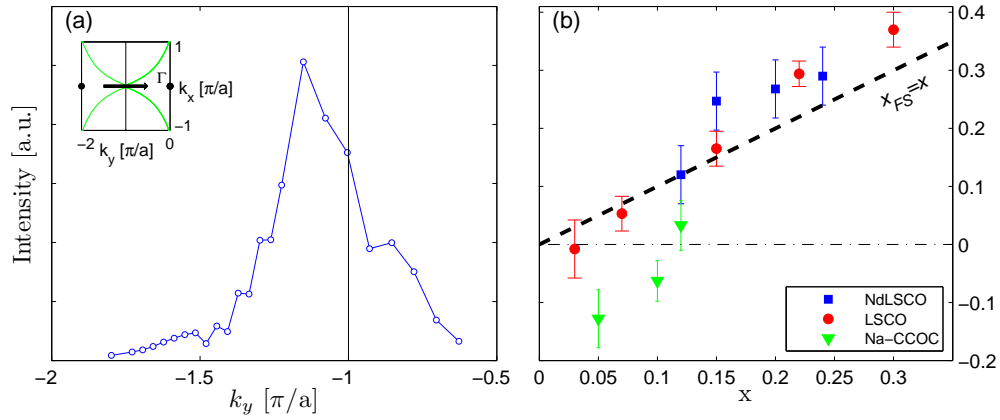


Figure 3.2: **a)** Intensity distribution along $(1, 0)$ as indicated by the black arrow in the inset. **b)** Doping and material dependence of the charge carrier number x_{FS} which reflects the Fermi surface area. Data on LSCO and Na-CCOC as presented by Yoshida [9], [17] show different behaviour. The dashed line reflects the expectation from Luttinger's theorem.

previously mentioned models which show small, hole like FS - pockets.

Chapter 4

The gap in the normal state

4.1 Introduction

A clue to resolve the microscopic mechanism driving unconventional superconductivity in cuprates is to understand the origin of the pseudogap phase [24, 31]. A substantial question in the field of cuprate superconductors is whether the pseudogap is a precursor to superconductivity with preformed cooper pairs but lacking phase coherence. In the low energetic excitation spectrum is characterized by a single gap. Or the pseudogap phase is a distinct, competing phase [21, 22] which introduces beside the superconducting gap a second energy scale for the pseudo gap. Since the discovery of this mysterious phase countless different experiments have been carried out to solve this problem; ending in contradicting explanations. In summary, both of the above mentioned scenarios is supported by a number of experiments which surprisingly can even base on the same technique; see for example reviews by Norman *et al.* [21], Hüfner *et al.* [22] or Millis *et al.* [23]. To mention the most prominent: Some experiments based on Nernst effect measurements [25, 26] and scanning tunneling spectroscopy (STS) [27] favor a one-gap scenario. The two-gap scenario is supported by resistivity measurements [4], Andreev reflection [29] and Raman scattering [30]. The above mentioned techniques, Nernst effect [31] and STS [32] also support in more recent experiments the competing scenario. ARPES is yet another technique, that has provided evidence in both directions. A similar temperature, momentum and doping dependence of the pseudogap and the superconducting gap [28, 33] fueled the idea that the pseudogap phase is a precursor to superconductivity. In two gap scenarios two distinct energy scales were observed which show different temperature- and k -dependent behaviour [34, 35, 36]. Confronted by these results we conclude that the doping and k -dependence of the gap size in the pseudogap phase (normal state) plays an essential role in describing the relationship between the superconducting phase and the pseudogap phase and in finding the description of the pseudogap phase.

In the following part of the report the lineshape and the gap size is investigated in the

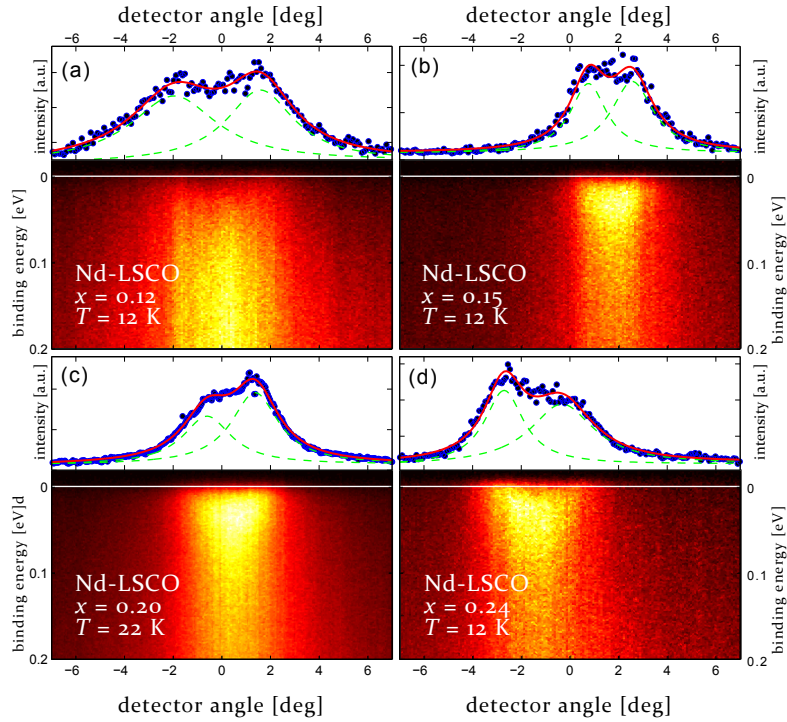


Figure 4.1: a)-d): ARPES intensity maps of antinodal cuts as indicated by the black line in the inset of figure e). On top of each spectra the MDC at the Fermi level integrated over an energyrange of ± 10 meV is shown. The MDC is fitted by a two- peak Lorentzian curve (red solid line) which is the sum of two single peak Lorentzian curves (green dashed lines). Values of \mathbf{k}_F are given by the peak position.

antinodal $(1,0)$ region where the magnitude of the pseudogap is maximum [2, 34, 38]. Also, ARPES measurements of the gap as function of the momentum k will be shown and compared to previous measurements. Finally, the behaviour of the pseudogap for different temperatures will be presented and discussed.

4.2 Lineshape of the the EDC in antinodal region

4.2.1 Antinodal ARPES spectra

Figures 4.1, a) - d) show ARPES cuts for $x = 0.12, 0.15, 0.20$ and 0.24 in the antinodal region along a cut parallel to the boundary of the Brillouin zone as indicated by the black line in the inset of figure 4.2 e). The raw spectra are presented as intensity maps as function of detector angle and binding energy E_b and are all measured in the normal state i.e. $T > T_c$ at temperatures as indicated. The calibration with respect to the Fermi level of polycrystalline copper and normalization to the background above E_F was done as described in section 2.3. The positions of the Fermi momenta \mathbf{k}_F were found by the MDC-method: The MDC, which is plotted on top of each spectrum was obtained by integration of spectral weight in a region

of ± 10 meV around E_F . By fitting a double Lorentzian on top of a first order polynomial background model (eq: 2.3) the peak positions of the MDC could be identified and assigned to \mathbf{k}_F .

4.2.2 Raw energy distribution curves

Extracted EDCs at one \mathbf{k}_F , in each case, are presented for $x = 0.12, 0.15, 0.20$ and 0.24 in figure 4.2. For $x = 0.15$ the lineshape (dashed line) is similar to that of $x = 0.20$. A spectral peak can be observed in the $x = 0.24$ sample which gets slightly suppressed and shifted to higher binding energies in the samples for $x = 0.20$ and 0.15 doping. The size and shape of this peak is in good agreement to normal state ($T > T_c$) measurements on LSCO ($\text{La}_{2-x}\text{Sr}_x\text{CuO}_4$) $x \approx 0.15$ [38, 43, 44] and slightly underdoped Bi2212, $p \approx 0.14$ [45]. The increase in size towards higher doping leads to the conclusion that this quasiparticle peak is of Fermi liquid like nature which describes the system in the metallic regime ($x \gtrsim 0.27$).

In the sample of $x = 0.12$, which is only slightly more underdoped than 0.15, the lineshape changed dramatically compared to the one for 0.15 and 0.20. The spectral peak gets entirely suppressed in a wide region below E_F and a kink can be observed at $\approx 30 \pm 5$ meV (indicated by the green vertical arrow). In this sample which shows no spectral peak, the position of the kink is interpreted as the onset of the pseudogap

[14] and therefore determines Δ^* . One reason for this strong suppression could lie in the phenomenon of charge and spin order within the copper planes around the $x = 1/8$ anomaly [4]. Around this doping, also superconductivity is strongly suppressed and the superconducting dome shows the characteristic dip. [39, 40]. In this so called stripe-phase state the dopant induced charge carriers spatially order in 2 dimensional stripes in a periodic fashion. These charge carriers exhibit higher binding energies leading to a depletion of particles around E_F . This new periodicity is accompanied by the opening of another gap and causes an additional suppression of particles in the vicinity of E_F [41].

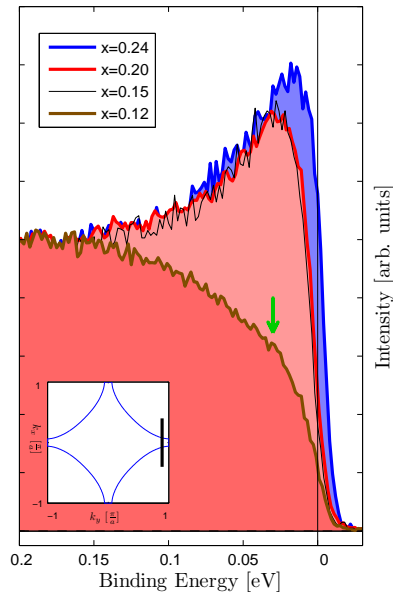


Figure 4.2: EDCs at selected Fermi momenta, \mathbf{k}_F , indicated in fig. 4.1 a)-d) in the antinodal region. The EDC for $x = 0.24$ (blue) shows the most pronounced quasiparticle peak. With underdoping ($x = 0.20$ and 0.15) the peak is suppressed by the pseudogap. For $x = 0.12$ the peak is completely suppressed due to stripe ordering [41] and the pseudogap is only visible in form of a kink (green arrow). The black line in the inset indicates the ARPES cut.

4.2.3 Symmetrized EDC - Analysis

For a quantitative gap-size analysis each EDC is symmetrized according to: $I_{\text{sym}}(\mathbf{k}, E) = I(\mathbf{k}, E) + I(\mathbf{k}, -E) = I_0(\mathbf{k})A(\mathbf{k}, E)$ (see eq: 2.6) to eliminate the Fermi distribution in the measured data. The data which is illustrated in figure 4.3 a) is fitted for $x = 0.15, 0.20, 0.24$ by use of the phenomenological self energy, equation 2.7, (Norman *et al.*; [37]) and illustrated by a solid black line. The extracted gap value is marked by the vertical black bars. In the case of $x = 0.12$ the black line is a guide to the eye and the exact gap value is adapted from Chang *et al.* [14]. The relevant characteristics like the kink in the $x = 0.12$ sample and the quasiparticle peak in the case of $x = 0.15, 0.20$ and 0.24 can also be identified in the symmetrized EDCs. While in the $x = 0.24$ sample the gap is entirely closed and the symmetrized spectrum results in a single peak, a gap opens for lower doping which increases towards lower doping. The extracted gap values are presented in table 4.1 and presented in the phase diagram of Nd-LSCO in a two Y-axis plot 4.3 by green circles. The left hand side (lhs) Y-axis (ordinate) indicates the energy of the gap while the right hand side (rhs) axis scales with the temperature. The superconducting dome (T_c , black solid line), is plotted with respect to the right (temperature indicating) axis. Similar to measurements in LSCO (Yoshida *et al.* [38]) the pseudogap size of Nd-LSCO Δ^* scales approximately with T^* following the mean field approximation $\Delta_{MF}^* = 4.3k_B T^*/2$ (Won *et al.* [46]). To calculate Δ_{MF}^* , values for T^* were adapted from the work by Daou *et al.* Δ_{MF}^* is illustrated by the blue solid line, calculated from T^* values which are summarized in Table 4.1. The phase diagram shows apparent (within the experimental resolution) that the pseudogap phase transition line is not gradually merging with the superconducting dome on the overdoped side but that the superconducting dome is cut by Δ^* .

	T_c [K]	T^* [K]	Δ^* [meV]
x = 0.12	3.5	155.4	30.0±5
x = 0.15	9.2	130.4	23.4±5
x = 0.20	19.0	80.0	19.4±5
x = 0.24	13.0	0.0	0±5

Table 4.1: Pseudogap size Δ^* for Nd-LSCO, $x = 0.12, 0.15, 0.20$ and 0.24 , extracted by use of the gapped Lorentzian function presented in eq. 2.7. The values of T_c and T^* are adapted from the work of Daou *et al.* [4].

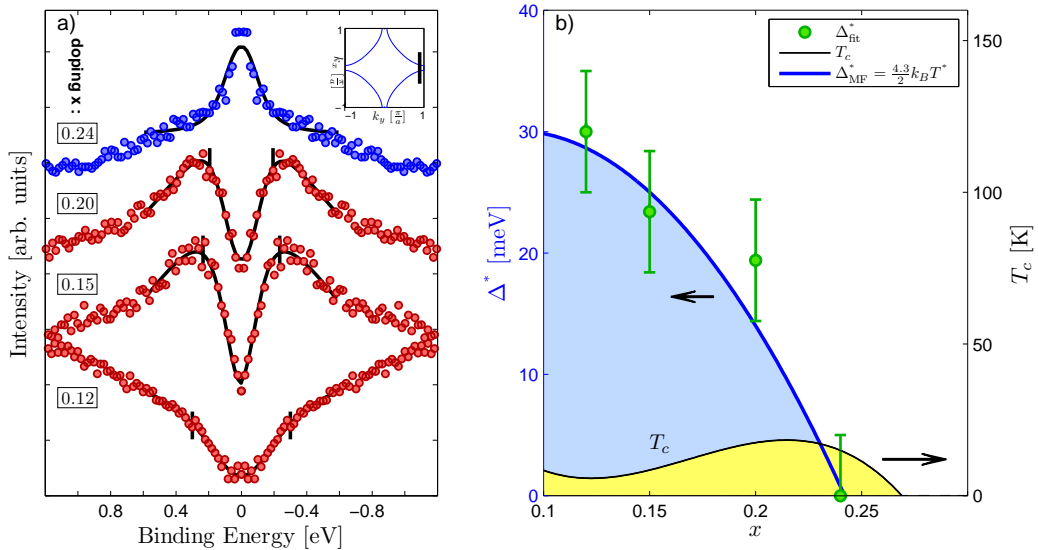


Figure 4.3: (a): Symmetrized EDC for Nd-LSCO, $x = 0.12$, $x = 0.15$, $x = 0.20$, $x = 0.24$ in the normal state (temp., see fig. 4.2). The measurement position (AN) in momentum space is sketched on the schematic Fermi surface in the inset of the figure. The symmetrized data is fitted by a phenomenological function [37] to extract the gap values for $x = 0.15$ and $x = 0.20$ as indicated by the vertical black bar. The gap value for $x = 0.12$ is adapted from [14]. (b): Two-axis phase diagram of Nd-LSCO. The measured pseudogap size Δ^* is plotted in form of green circles and referring to the left hand side. The superconducting dome (black solid line) is drawn with respect to the right hand side axis. The blue line is the mean field expectation $\Delta^* = 4.3k_B T^*/2$ (Won *et al.*, [46])

4.3 Momentum dependence of the pseudogap

For further analysis of the interplay between pseudogap and superconductivity and their individual dominance in different momentum space regions, the k -dependence of the normal-state gap size of Nd-LSCO $x = 0.20$ will be presented. A comparison to studies by Chang *et al.* [14] on Nd-LSCO $x = 0.12$ reveals a similar evolution of the Fermi arc of gapless quasiparticle dispersion as seen in other cuprate compounds like Bi2212 by Lee *et al.* or LSCO [38, 43, 34]. In these studies an increasing Fermi arc length is seen towards higher doping. In contrast to these and our results, measurements on $\text{La}_{2-x}\text{Ba}_x\text{CuO}_4$ (LBCO) revealed a $d_{x^2-y^2}$ -wave (d -wave) gap in the normal state [33]. A gap with a d -wave form only vanishes at the nodal points.

Our measurements on the normal state gap size for $x = 0.20$ as function of the Fermi surface angle φ are presented in figure 4.5. Symmetrized EDC (panel (a)) at different FS angles (indicated in (c)) are fitted by the previously mentioned phenomenological function (Norman *et al.*) to extract the size of Δ^* (indicated by vertical markers). The result is summarized in panel (b) by red and blue circles (finite gap size / gapless spectra) illustrating Δ^* versus φ . Data for $x = 0.12$ is taken from Chang *et al.* and for direct comparison replotted in panel (d). Chang *et al.* found the pseudogap vanishing for $\varphi \geq 33.2 \pm 7.7^\circ$ while we measure

gapless EDC at angles $\varphi \geq 30.7 \pm 4.2^\circ$ in the compound for $x = 0.20$.

A comparison with different cuprate compounds in figure 4.4 for different hole doping values affirms the trend to increasing Fermi arc length K_a for increasing hole doping x . This can be interpreted, in accordance with the increase of the quasiparticle peak, as a trend of the system to follow more and more the description by Fermi-liquid theory and dive into the metallic region in the phase diagram. However, a finite Fermi arc length K_a is in sharp contrast to the momentum dependence of the Fermi arc of the superconducting (SC) gap which shows no doping evolution. The superconducting gap is assumed to follow simple d -wave behaviour for all doping values [47, 44, 34, 49] (dashed black line in figure 4.5, (b)/(d)) and vanishes only in one point in the node.

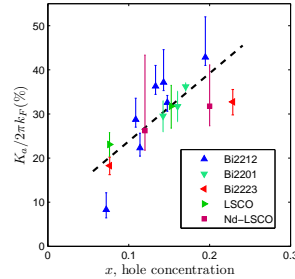


Figure 4.4: Fermi arc length K_a for different cuprate compounds and dependent on the hole concentration x relative to the full Fermi surface $2\pi k_F$. Data for compounds except Nd-LSCO is adapted from Yoshida *et al.* [34] and replotted. Nd-LSCO data is taken from our measurement. Dashed line is a guide to the eye.

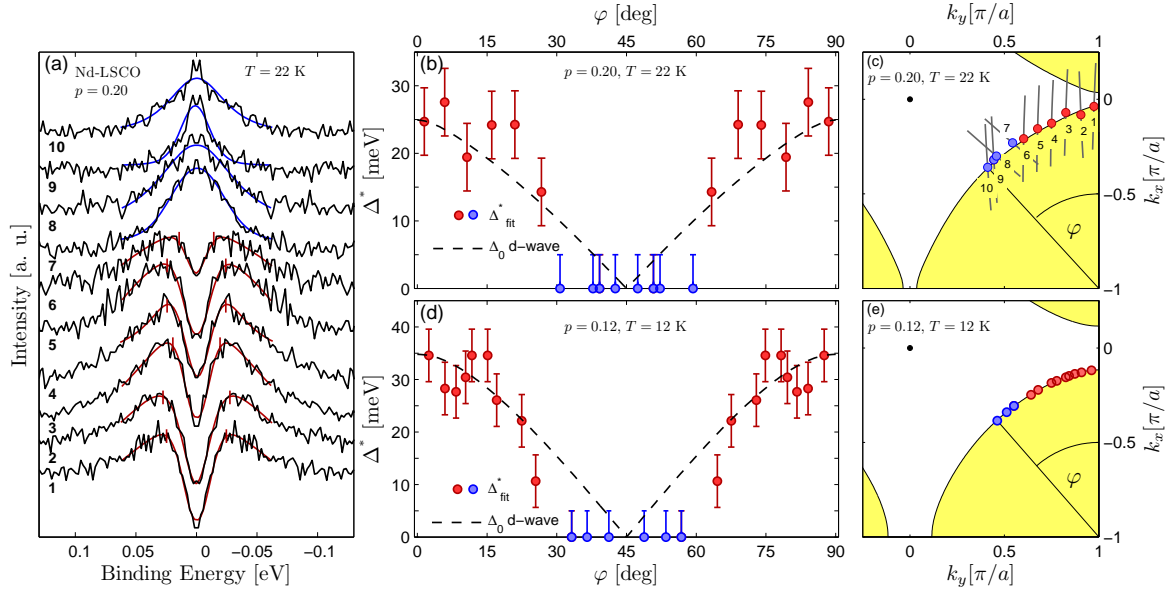


Figure 4.5: (a): Black curve: Symmetrized EDC curves for different Fermi surface angles φ (figure (e)) from the antinode (1) to the node (10) for $x = 0.20$ ($T_c \approx 19$ K) measured in the normal state ($T = 22$ K). Red/blue curve: Fit of the symmetrized EDC by a phenomenological function as proposed by Norman *et al.* [37]. Vertical lines indicate the extracted gap values. Red curve indicates gapped EDCs while blue stands for EDC without gap. (b) (d): Extracted gap values Δ^* as indicated by vertical lines in (a) for $x = 0.20$ and adapted from Chang *et al.* [14] for $x = 0.12$, as function of the Fermi surface angle φ . The dashed black lines represent the d-wave form of the superconducting gap value. (c),(e) Fermi surface for $x = 0.20$ / $x = 0.12$. Blue/red dots indicate the position of \mathbf{k}_F of gapped/ungapped spectra in (a),(b)/(e). The cut of the $x = 0.20$ -ARPES spectra was taken along the grey lines in (c).

4.4 Temperature dependence of the pseudogap

4.4.1 Introduction

In previous sections we discussed the measurements on doping and k -dependence of the pseudogap Δ^* in normal state. In this section, a temperature dependent study of the pseudogap of the $x = 0.20$ sample completes this report about investigations on the pseudogap phase in Nd-LSCO.

Previous ARPES studies of the pseudogap as a function of temperature have been interpreted differently. In one scenario the pseudogap size is gradually decreasing as the T approaches T^* [2, 49, 50]. In these studies the gap size was measured by the leading edge (LEM) shift with respect to the Fermi level. In a second scenario, the pseudogap is extracted by the EDC peak displacement with respect to an ungapped spectrum. In this scenario, Δ^* is not decreasing successively but abruptly vanishes near T^* [51, 52, 53]. A common finding by all of these studies was the phenomenon of successive ‘filling-in’ due to growth of in-gap states (see also Kanigel *et al.* [52], Matsui *et al.* [55] and others [51, 54]).

4.4.2 Result: Δ^* in Nd-LSCO, $x = 0.20$

Our temperature dependent measurements in the antinodal region of Nd-LSCO, $x = 0.20$ in the normal state are presented in fig. 4.7. Panel (a) shows symmetrized EDCs extracted at \mathbf{k}_F (see panel (b)) for different temperatures as indicated. For temperatures lower than 80 K, a two-peak structure was observed. This was taken as clear evidence for a gap in the excitation spectrum. If the gap size Δ^* is defined by the maximum position (green arrows) an abrupt closing of the gap could be observed. A gap of size $\Delta^*(T) \gtrsim 20 \pm 5$ meV for temperatures up to $T = 70$ K vanishes within a range of 10 K, compatible with the above mentioned filling-in of the ingapped states which also applies to our measurements. This allowed us to define the pseudogap onset temperature $T^* = 80 \pm 10$ K for this sample. This is in excellent agreement with resistivity measurements presented in fig. 1.1.

4.4.3 Analysis

In order to use a consistent way of extracting the gap value Δ^* throughout the whole report, the low energetic spectral weight was fitted by the resolution broadened spectral function as introduced in section 2.4.1. Black vertical lines indicate the obtained values of Δ^* . While the gap was open for temperatures below 80 K and two peaks could be observed, for $T = 80$ K the gap entirely closed and one single spectral peak occurred in the symmetrized EDC. In panel (c), $\Delta^*(T)$ is plotted against the temperature T . The black dashed line marks the BCS prediction. This way of analysis revealed that $\Delta^*(T)$ remained unchanged for a large temperature range $T \lesssim 50$ K and gradually closed above 50 K for $T \rightarrow T^*$. Compared to the values which were given by the peak maxima, a much less abrupt closing of the gap could be observed.

4.4.4 Vacuum issues and self surface doping

As mentioned previously (section 1.2), ARPES is an extremely surface sensitive technique. Ultra high vacuum (UHV) conditions (pressure of less than 10^{-10} Torr) have to remain constant inside the measurement chamber to prevent the surface state and surface doping being changed by contaminants. This effect is usually called surface aging. A measure for the degree of surface aging is given by the size of the gap [56]. Figure 4.6 illustrates the symmetrized EDC before heating the sample and afterwards. Both EDCs are measured at base

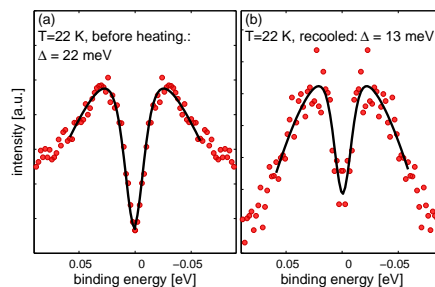


Figure 4.6: (a): Pseudogap before heating the sample. The gap size is 22 meV. (b) Recooled after T -dependent measurement. $\Delta^* = 13$ meV.

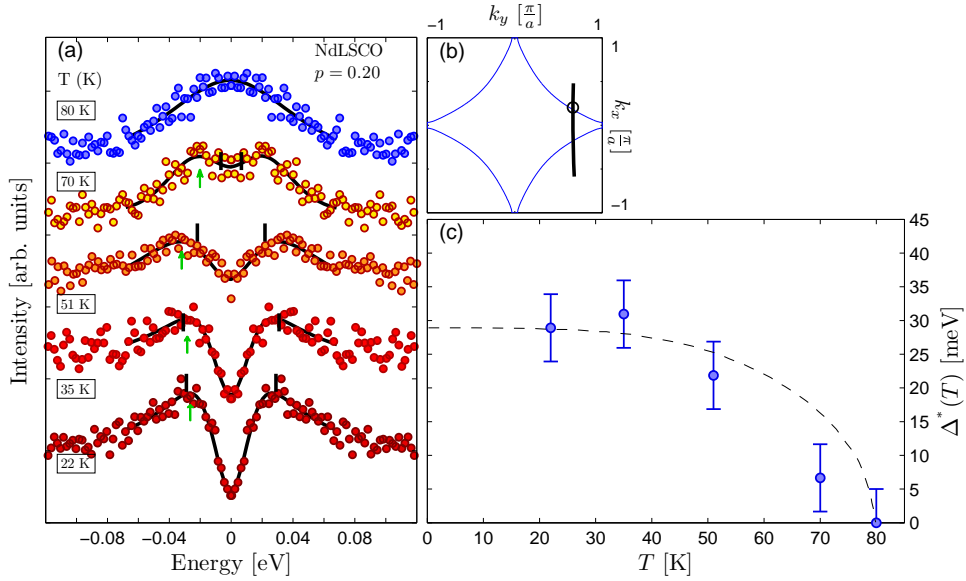


Figure 4.7: (a): Symmetrized EDCs in the antinodal region at \mathbf{k}_F , indicated by the black circle in (b) for Nd-LSCO $x = 0.20$ at different temperatures. The fit by the phenomenological function of Norman *et al.* (black line) reveals the gap value Δ^* which is shown by vertical bars. (b): Tight-binding model of the FS for $x = 0.20$. The black circle indicates the measurement position of the symmetrized EDC presented in (a). (c): Δ^* vs. temperature T . The black line indicates the expectation by BCS theory (adapted from [48]).

temperatures ($T = 22$ K). As indicated in the plot, the gap size of the recooled EDC was approximately half the size of the initial gap value. To estimate a rough value for the change of the surface doping a simple linear gap-vs-doping dependence was assumed. Conclusively, the surface doping was given by $x = 0.20 \pm 0.02$.

4.4.5 Outlook

In order to find a description of the microscopic mechanism of the pseudogap state the question of the broken symmetry when cooling into the pseudogap phase arises. Recent reports on single-layered Pb-Bi2201 ($\text{Pb}_{0.55}\text{Bi}_{1.5}\text{Sr}_{1.6}\text{La}_{0.4}\text{CuO}_{6+\delta}$) [57, 58] conclude a particle hole symmetry breaking at the transition to the pseudogap phase at T^* . The conclusion was drawn on the observation of an abrupt change of \mathbf{k}_F when cooling below T^* . In the limited time for this master project, we couldn't succeed to observe a relevant change in \mathbf{k}_F within small enough error bars. Improved experimental conditions might solve this problem and allow us to make reasonable conclusions.

Chapter 5

Conclusion

The pseudogap phase, characteristic for high- T_c cuprate superconductors, was investigated by angle resolved photoemission spectroscopy (ARPES). The measurements were done on single crystalline $\text{La}_{1.6-x}\text{Nd}_{0.4}\text{Sr}_x\text{CuO}_4$ in a wide doping range between $x = 0.12$ and 0.24 in the normal state ($T > T_c$).

Underlying Fermi surface: In a first step, the underlying Fermi surface (FS) was measured. Similar to measurements in LSCO [9] the underlying Fermi surface was of large, hole like character for $x = 0.15$, centered around (1,1) and of large, electron like character for $x = 0.24$, centered around (0,0). We concluded that the transition from hole to electron like has to be at a doping around $x = 0.20$. A tight binding (TB) model was used to fit and parametrize the FS topology. In this fashion the FS area was derived and compared to results obtained for LSCO [9] which show similar behaviour and also follow quite reasonable the expectation by Luttinger's sum rule (see fig. 5.1, (a)).

Momentum dependence: Connected to the Fermi surface is the question of the Fermi arc. The Fermi arc is defined by the locus of \mathbf{k}_F -points in momentum space where the quasi-particle excitations in normal state are gapless. As summarized in figure 5.1, (b), the length of the Fermi arc, K_a , is found to increase with increasing doping, consistent with various other hole doped cuprate compounds. The finite length of the Fermi arc in normal-state is in big contrast to the momentum dependence in the superconducting phase where the gap anisotropy shows d -wave form and the gap vanishes only in the nodal point. This difference of the gap-momentum dependence for different dopings between the superconducting and the normal (pseudogap) phase is a clear indication of their different microscopic origin and allots the pseudogap phase to a competing phase.

Temperature dependence: Studying the pseudogap size for the sample of $x = 0.20$ (shown in panel (c)) lead to further characterization of the the pseudogap state and revealed T^* for $x = 0.20$.

Antinodal lineshape: Finally, to complement the phase diagram of Nd-LSCO, the pseudogap size and the EDC - lineshape were studied in the antinodal region around (1, 0) where the pseudogap is most distinctive. A gradual closing of the gap could be observed towards

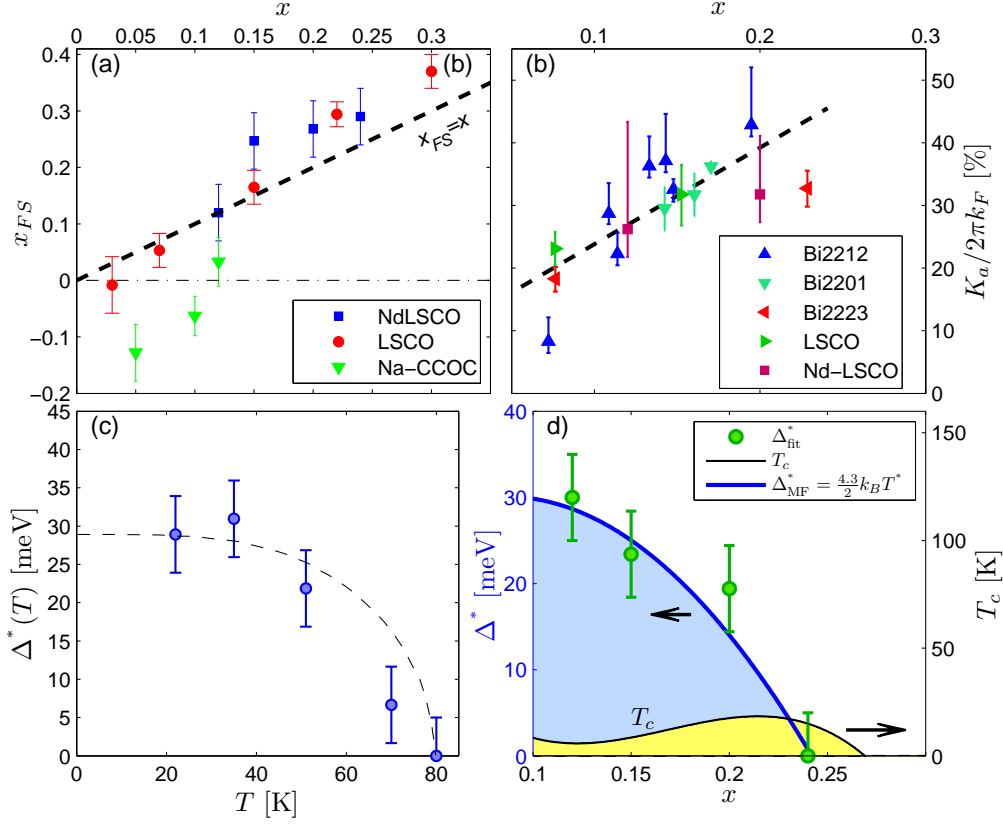


Figure 5.1: (a): Fermi surface volume x_{FS} for different doping and different cuprate compounds. Black dashed line illustrates the expectation of Luttinger's theorem. (b): Length of Fermi arc K_a normalized to total circumference of the Brillouin zone for different cuprate compounds. Dashed black line is a guide to the eye. (c): Temperature dependence of the pseudogap size Δ^* for Nd-LSCO, $x = 0.20$. Dashed black line indicates the expectation of BCS theory. (d): Resulting cuprate phasediagram. Green circles: Measured pseudogap size Δ^* ; Blue line: Mean field expectation of pseudoap size $\Delta^* = 4.3/2k_B T^*$ [46]. T^* is adapted from [4]. Black line: T_c , adapted from [4].

higher doping, vanishing in the sample with $x = 0.24$ which still exhibits superconductivity (fig: 5.1 (d)). This, again, leads us to the conclusion that the pseudogap phase cannot be a pre-superconducting phase. The study of the doping dependence of the normal state gap size revealed, similar to observations in $\text{La}_{2-x}\text{Sr}_x\text{CuO}_4$ (LSCO), a linear scaling dependence between the pseudogap size Δ^* and the pseudogap transition temperature T^* , $\Delta_{MF}^* = 4.3k_B T^*/2$, as predicted by mean field calculations by Won *et al.* [46] Previous measurements concerning particle-hole symmetry breaking when cooling into the pseudogap phase [57, 58] (crossing T^*) could, so far, not conclusively be observed in Nd-LSCO and remain a matter of future interest. The observation of a broken symmetry, characteristic for the pseudogap phase, would contain a big amount of physical information about the underlying microscopic mechanism and therefore is of great interest.

Bibliography

- [1] Bednorz J.G., Müller K.A.; Possible High Tc superconductivity in the Ba-La-Cu-O; Z.Phys. B Cond. Matter 64, 189-193 (1986).
- [2] A. Damascelli, Z. Hussain, Z.X. Shen; Angle-resolved photoemission studies of the cuprate superconductors; Rev. Mod. Phys. 75, 473 (2003).
- [3] J. Bardeen, L. N. Cooper, and J. R. Schrieffer. Theory of superconductivity. Phys. Rev., 108(5):1175-1204, (1957)
- [4] R. Daou, N. Doiron-Leyraud, D. LeBoeuf, S. Y. Li, F. Lalibert, O. Cyr-Choinire, Y. J. Jo, L. Balicas, J.-Q. Yan, J.-S. Zhou, J. B. Goodenough, L. Taillefer; Linear temperature dependence of resistivity and change in the Fermi surface at the pseudogap critical point of a high-Tc superconductor; Nature Phys. 5, 31 (2008)
- [5] N. Momono, T. Matsuzaki, M.Oda, M. Ido; Superconducting Condensation Energy and pseudogap Formation in $\text{La}_{2-x}\text{Sr}_x\text{CuO}_4$: New Energy scale for Superconductivity, J. Phys. Soc.Jpn. 71, 2832 (2002).
- [6] B. Vignolle ,A. Carrington, R.A. Cooper, M.M. J. French, A. P.Mackenzie, C. Jaudet, D. Vignolles, Cyril Proust, N. E. Hussey; Quantum oscillations in an overdoped high-Tc superconductor; Nature 455, 952 (2008).
- [7] M. Plate, J.D. F. Mottershead, I. S. Elfimov, D.C. Peets, Ruixing Liang, D.A. Bonn, W.N. Hardy, S. Chiuzaian, M. Falub, M. Shi, L. Patthey, and A. Damascelli; Fermi Surface and Quasiparticle Excitations of Overdoped $\text{Tl}_2\text{Ba}_2\text{CuO}_{6-\delta}$; Phys. Rev. Lett. 95, 077001 (2005).
- [8] O. K. ANDERSEN, A. I. LIECHTENSTEIN, O. JEPSSEN and E. PAULSEN; LDA ENERGY BANDS, LOW-ENERGY HAMILTONIANS, $t, t, t_{\perp}(\mathbf{k})$, and J_{\perp} ; J. Phys. Chem. Solids 56, 15731591 (1995).
- [9] T. Yoshida, X. J. Zhou, K. Tanaka, W. L. Yang, Z. Hussain, Z.-X. Shen, A. Fujimori, S. Sahrakorpi, M. Lindroos, R. S. Markiewicz, A. Bansil, S. Komiya, Y. Ando, H. Eisaki, T. Kakeshita, S. Uchida; Systematic doping evolution of the underlying Fermi surface of $\text{La}_{2-x}\text{Sr}_x\text{CuO}_4$; Phys. Rev. B. 74, 224510 (2006).

- [10] J.M. Luttinger, Fermi Surface and Some Simple Equilibrium Properties of a System of Interacting Fermions, *Phys. Rev.* 119, 1153 (1960).
- [11] N. Doiron-Leyraud, C. Proust, D. LeBoeuf, J. Levallois, J.-B. Bonnemaïson, R. Liang, D. A. Bonn, W. N. Hardy, L. Taillefer; Quantum oscillations and the Fermi surface in an underdoped high-Tc superconductor; *Nature* 447, 565 (2007).
- [12] Cyril Jaudet, Julien Levallois, Alain Audouard, David Vignolles, Baptiste Vignolle, Ruixing Liang, D.A. Bonn, W.N. Hardy, N.E. Hussey, Louis Taillefer, Cyril Proust; Quantum oscillations in underdoped $\text{YBa}_2\text{Cu}_3\text{O}_{6.5}$; *Physica B* 404 3546 (2009).
- [13] J. Meng, G. Liu, W. Zhang, L. Zhao, H. Liu, X. Jia, D. Mu, S. Liu, X. Dong, J. Zhang, W. Lu, G. Wang, Y. Zhou, Y. Zhu, X. Wang, Z. Xu, C. Chen, X. J. Zhou; Coexistence of Fermi arcs and Fermi pockets in a high-Tc copper oxide superconductor; *Nature* 462, 335 (2009)
- [14] J. Chang, Y. Sassa, S. Guerrero, M. Månsson, M. Shi, S. Pailhs, A. Bendounan, R. Mottl, T. Claesson, O. Tjernberg, L. Patthey, M. Ido, M. Oda, N. Momono, C. Mudry, J. Mesot; Electronic structure near the 1/8-anomaly in La-based cuprates; *N. J. Phys.* 10, 103016 (2008).
- [15] A. J. Millis, M. R. Norman; Antiphase stripe order as the origin of electron pockets observed in 1/8-hole-doped cuprates; *Phys. Rev. B* 76, 220503(R) (2007).
- [16] Louis Taillefer; Fermi surface reconstruction in high-Tc superconductors; *J. Phys.:Condens. Matter* 21 164212 (2009)
- [17] Kyle M. Shen, F. Ronning, D. H. Lu, F. Baumberger, N. J. C. Ingle, W. S. Lee, W. Meevasana, Y. Kohsaka, M. Azuma, M. Takano, H. Takagi, Z.-X. Shen; nodal Quasiparticles and antinodal Charge Ordering in $\text{Ca}_{2x}\text{Na}_x\text{CuO}_2\text{Cl}$; *Science* 307, 901 (2005).
- [18] S. V. Borisenko, A. A. Kordyuk, S. Legner, C. Dürr, M. Knupfer, M. S. Golden, and J. Fink; Estimation of matrix-element effects and determination of the Fermi surface in $\text{Bi}_2\text{Sr}_2\text{CaCu}_2\text{O}_{8+\delta}$ systems using angle-scanned photoemission spectroscopy; *Phys. Rev. B* 64, 094513 (2001).
- [19] N. Ichikawa, S. Uchida, J.M. Tranquada, T. Niemöller, P.M. Gehring, S.-H. Lee, J.R. Schneider; Local Magnetic Order vs Superconductivity in a Layered Cuprate; *PRL* 85, 8, 1738 (2000).
- [20] T. Yoshida, X. J. Zhou, M. Nakamura, S. A. Kellar, P. V. Bogdanov, E. D. Lu, A. Lanzara, Z. Hussain, A. Ino, T. Mizokawa, A. Fujimori, H. Eisaki, C. Kim, Z.-X. Shen, T. Kakeshita, S. Uchida; Electronlike Fermi surface and remnant $(\pi, 0)$ feature in overdoped $\text{La}_{1.78}\text{Sr}_{0.22}\text{CuO}_4$; *Phys. Rev. B* 63, 220501 (R) (2001).

- [21] M. R. Norman, D. Pines, C. Kallin; The pseudogap: friend or foe of high T_c ?; Adv. in Phys. 54, 8, 715-733 (2005).
- [22] S. Hufner, M. A. Hossain, A. Damascelli, G. A. Sawatzky; Two gaps make a high-temperature superconductor?; Rep. Prog. Phys. 71 062501 (2008).
- [23] A. J. Millis; Gaps and Our Understanding; Science 314, 1888 (2006)
- [24] A. Cho; High T_c : The Mystery That Defies Solution; Science 314, 1072 (2006)
- [25] Z. A. Xu, N. P. Ong, Y. Wang, T. Kakeshita, S. Uchida; Vortex-like excitations and the onset of superconducting phase fluctuation in underdoped $La_{2-x}Sr_xCuO_4$; Nature, 406, 486 (2000).
- [26] Y. Wang, Lu Li, N. P. Ong; Nernst effect in high- T_c superconductors; Phys. Rev. B. 73, 024510 (2006).
- [27] Ch. Renner, B. Revaz, J.-Y. Genoud, K. Kadowaki, O. Fischer; pseudogap Precursor of the Superconducting Gap in Under- and Overdoped $Bi_2Sr_2CaCu_2O_{8+d}$; Phys. Rev. Lett. 80, 1, 149 (1998).
- [28] M. Shi, A. Bendounan, E. Razzoli, S.Rosenkranz ,M.R.Norman, J. C. Campuzano, J. Chang, M. Mansson, Y.Sassa, T.Claesson, O.Tjernberg, L.Patthey, N. Momono, M.Oda, M.Ido, S. Guerrero, C.Mudry, J. Mesot; Spectroscopic evidence for preformed Cooper pairs in the pseudogap phase of cuprates; EPL, 88 27008 (2009).
- [29] V. M. Svistunov, V. Yu. Tarenkov, A. I. Dyachenko, and E. Hatta; Temperature Dependence of the Energy Gap in Bi2223 Metal Oxide Superconductor; JETP Lett. 71 289 (2000).
- [30] T. P. Devereaux, R. Hackl; Inelastic light scattering from correlated electrons; Rev. Mod. Phys. 79 175 (2007).
- [31] J. Chang, Nicolas Doiron-Leyraud, Francis Laliberte, R. Daou, David LeBoeuf, B. J. Ramshaw, Ruixing Liang, D. A. Bonn, W. N. Hardy, Cyril Proust, I. Sheikin, K. Behnia, Louis Taillefer; Nernst effect in the cuprate superconductor $YBa_2Cu_3O_y$: Broken rotational and translational symmetry; PHY. REV. B 84, 014507 (2011)
- [32] M Oda, Y H Liu, T Kurosawa, K Takeyama, N Momono and M Ido; On the relations among the pseudogap, electronic charge order and Fermi-arc superconductivity in $Bi_2Sr_2CaCu_2O_{8+d}$; J. of Phys.: Conf. Ser 108 012008(2008);
- [33] T. Valla, A. V. Fedorov, Jinho Lee, J. C. Davis, G. D. Gu; The Ground State of the pseudogap in Cuprate Superconductors; Science 314, 1914 (2006).
- [34] T. YOSHIDA, M. HASHIMOTO, I. M. VISHIK, Z.-X. SHEN, and A. FUJIMORI; pseudogap, Superconducting Gap, and Fermi Arc in High-Tc Cuprates Revealed by Angle-Resolved Photoemission Spectroscopy; J. Phys. Soc. Jpn. 81, 011006 (2012).

- [35] I. M. Vishik, W. S. Lee, R.-H. He, M. Hashimoto, Z. Hussain, T. P. Devereaux, Z.-X. Shen; ARPES studies of cuprate Fermiology: superconductivity, pseudogap and quasiparticle dynamics; *N. J. Phys.* 12 105008 (2010).
- [36] C. Matt; Semesterthesis: Origin of the pseudogap phase in La-based cuprates; PSI 2011
- [37] M. R. Norman, M. Randeria, H. Ding, J. C. Campuzano; Phenomenology of the low-energy spectral function in high-Tc superconductors; *Phys. Rev. B* 57, 18, R11094 (1998).
- [38] T. Yoshida, M. Hashimoto, S. Ideta, A. Fujimori, K. Tanaka, N. Mannella, Z. Hussain, Z.-X. Shen, M. Kubota, K. Ono, Seiki Komiya, Yoichi Ando, H. Eisaki, S. Uchida; Universal versus Material-Dependent Two-Gap Behaviors of the High-Tc Cuprate Superconductors: Angle-Resolved Photoemission Study of $\text{La}_{2-x}\text{Sr}_x\text{CuO}_4$; *Phys. Rev. Let.* 103, 037004 (2009).
- [39] J. M. Tranquada, J. D. Axe, N. Ichikawa, Y. Nakamura, S. Uchida, B. Nachumi; Neutron-scattering study of stripe-phase order of holes and spins in $\text{La}_{1.48}\text{Nd}_{0.4}\text{Sr}_{0.12}\text{CuO}_4$; *Phys. Rev. B*, 54,10, 7489 (1996).
- [40] J. M. Tranquada, N. Ichikawa, S. Uchida; Glassy nature of stripe ordering in $\text{La}_{1.6-x}\text{Nd}_{0.4}\text{Sr}_x\text{CuO}_4$; *Phys. Rev. B*, 59 22 14712 (1999).
- [41] Tranquada J.M. , Sternlieb B.J., Axe J.D., Nakamura Y., Uchida S.; Evidence for stripe correlations of spins and holes in copper oxide superconductor; *Nature* 375, 561 (1995).
- [42] Kiyohisa Tanaka, W. S. Lee, D. H. Lu, A. Fujimori, T. Fujii, Risdiana, I. Terasaki, D. J. Scalapino, T. P. Devereaux, Z. Hussain, Z.-X. Shen; Distinct Fermi-Momentum-Dependent Energy Gaps in Deeply Underdoped Bi2212; *Science* 314, 1910 (2006)
- [43] K. Terashima, H. Matsui, T. Sato, T. Takahashi, M. Kofu, K. Hirota; Anomalous Momentum Dependence of the Superconducting Coherence Peak and Its Relation to the pseudogap of $\text{La}_{1.85}\text{Sr}_{0.15}\text{CuO}_4$; *PRL* 99, 017003 (2007).
- [44] M. Shi, J. Chang, S. Pailhs, M.R. Norman, J.C. Campuzano, M.Mansson, T. Claesson, O. Tjernberg, A. Bendounan, L. Patthey, N. Momono, M. Oda, M. Ido, C. Mudry, J. Mesot; Coherent d-Wave Superconducting Gap in Underdoped $\text{La}_{2-x}\text{Sr}_x\text{CuO}_4$ by Angle-Resolved Photoemission Spectroscopy
- [45] W. S. Lee, I. M. Vishik, K. Tanaka, D.H.Lu, T. Sasagawa, N. Nagaosa, T. P. Devereaux, Z. Hussain, Z.-X. Shen; Abrupt onset of a second energy gap at the superconducting transition of underdoped Bi2212; *Nature* 450, 81 (2007).
- [46] H. Won, K. Maki; D-wave superconductor as a model of high-T, superconductors; *Phys. Rev. B*, 49, 2, 1397 (1994);

- [47] S. I. Ideta, T. Yoshida, A. Fujimori, H. Anzai, T. Fujita, A. Ino, M. Arita, H. Namatame, M. Taniguchi, Z.-X. Shen, K. Takashima, K. Kojima, S.-I. Uchida; Energy scale directly related to superconductivity in high- T_c cuprates: Universality from the temperature-dependent angle-resolved photoemission of $\text{Bi}_2\text{Sr}_2\text{Ca}_2\text{Cu}_3\text{O}_{10+\delta}$; *Phys. Rev. B* 85, 104515 (2012).
- [48] I. Giaever, K. Megerlk; Study of Superconductors by Electron Tunneling; *Phys. Rev.* 122,4; 1961
- [49] H. Ding, T. Yokoya, J.C. Campuzano, T. Takahashi, M. Randeria, M.R. Norman, T. Mochiku, K. Kadowaki, J.Giapintzakis; Spectroscopic evidence for a pseudogap in the normal state of underdoped high- T_c superconductors; *Nature* 382, 51 (1996).
- [50] J. M. Harris, Z.-X. Shen, P. J. White, D. S. Marshall, and M. C. Schabel, J. N. Eckstein and I. Bozovic; Anomalous superconducting state gap size versus T_c behavior in underdoped $\text{Bi}_2\text{Sr}_2\text{Ca}_{1-x}\text{Dy}_x\text{Cu}_2\text{O}_{8+\delta}$; *Phys. Rev. B*, 54 R15665 (1996).
- [51] T. Timusk, and B. Statt; The pseudogap in high-temperature superconductors: an experimental survey; *Rep. Prog. Phys.* 62, 61 (1999).
- [52] A. Kanigel, M.R. NORMAN, M.RANDERIA, U. CHATTERJEE, S.SOUMA, A. KAMINSKI, H. M. FRETWELL, S.ROSENKRANZ, M.SHI, T.SATO, T. TAKAHASHI, Z.Z.LI, H.RAFFY, K. KADOWAKI, D.HINKS, L. OZYUZER, J.C.CAMPUZANO; Evolution of the pseudogap from Fermi arcs to the nodal liquid; *Nat. Phys.* 2, 447 (2006)
- [53] Competition between the pseudogap and superconductivity in the high- T_c copper oxides; *Nature* 457, 296 (2009)
- [54] M. R. Norman, H. Ding, M. Randeria, J. C. Campuzano, T. Yokoya, T. Takeuchi, T. Takahashi, T. Mochiku, K. Kadowaki, P. Guptasarma, D. G. Hinks; Destruction of the Fermi surface in underdoped high- T_c superconductors; *Nature* 392, 157 (1998).
- [55] H. Matsui, T. Takahashi, T. Sato, K. Terashima, H. Ding, T. Uefuji, K. Yamada; Evolution of the pseudogap across the magnet-superconductor phase boundary of $\text{Nd}_{2-x}\text{Ce}_x\text{CuO}_4$; *Phys. Rev. B.* 75 224514 (2007).
- [56] A. D. Palczewski, T. Kondo, J. S. Wen, G. Z. J. Xu, G. Gu, A. Kaminski; Controlling the carrier concentration of the high-temperature superconductor $\text{Bi}_2\text{Sr}_2\text{CaCu}_2\text{O}_{8+\delta}$ in angle-resolved photoemission spectroscopy experiments; *Phys. Rev. B*, 81, 104521 (2010).
- [57] Rui-Hua He, M. Hashimoto, H. Karapetyan, J. D. Koralek, J. P. Hinton, J. P. Testaud, V. Nathan, Y. Yoshida, Hong Yao, K. Tanaka, W. Meevasana, R. G. Moore, D. H. Lu, S.-K. Mo, M. Ishikado, H. Eisaki, Z. Hussain, T. P. Devereaux, S. A. Kivelson, J. Orenstein, A. Kapitulnik, Z.-X. Shen; From a Single-Band Metal to a High-Temperature Superconductor via Two Thermal Phase Transitions; *Science*, 331, 1579 (2011).

- [58] Makoto Hashimoto, Rui-Hua He, K. Tanaka, J. P. Testaud, W. Meevasana, R. G. Moore, D. Lu, Hong Yao, Y. Yoshida, H. Eisaki, T. P. Devereaux, Z. Hussain, Z.-X. Shen; Particlehole symmetry breaking in the pseudogap state of Bi2201; Nat. Phys., 6, 414 (2010).
- [59] Chang, J. MAGNETIC AND ELECTRONIC PROPERTIES OF THE HIGH-TEMPERATURE SUPERCONDUCTOR $\text{La}_{2-x}\text{Sr}_x\text{CuO}_4$, Dissertation, 2008
- [60] <http://www.ifp.uni-bremen.de/uploads/images/Surface/arpes.png>
- [61] Stefan Hüfner; Photoelectron spectroscopy; 2nd Edition, Springer-Verlag New York, 1995.
- [62] C. N. Berglund, W. E. Spicer; Photoemission Studies of Copper and Silver: Theory; Phys. Rev. 136, A1030A1044 (1964).
- [63] W. Schattke et al., 2003, Solid-State Photoemission and Related Methods, 2003 WILEY-VCH GmbH & Co.KGaA
- [64] Courtesy of Dr. Yasmine Sassa, ARPES Investigations on in situ PLD grown $\text{YBa}_2\text{Cu}_3\text{O}_{7-\delta}$, Neuchâtel, 2011.
- [65] J. Minar, J. Braun, S. Mankovsky, H. Ebert; Calculation of angle-resolved photo emission spectra within the one-step model of photo emission Recent developments; Journal of Electron Spectroscopy and Related Phenomena 184, 9199, (2011).
- [66] R4000 data sheet v3.5 + model overview v1.4 web.pdf
- [67] <http://hoffman.physics.harvard.edu/materials/images/lSCO.gif> (29.6.2012).
- [68] A. Kaminski, S. Rosenkranz, H. M. Fretwell, J. Mesot, M. Randeria, J. C. Campuzano, M. R. Norman, Z. Z. Li, H. Raffy, T. Sato, T. Takahashi, K. Kadowaki; Identifying the background signal in angle-resolved photoemission spectra of high-temperature cuprate superconductors; Phys. Rev. B 69, 212509 (2004).